Cathodoluminescence features, trace elements, and oxygen isotopes of quartz in unidirectional solidification textures from the Sn-mineralized Heemskirk Granite, western Tasmania

Wei Hong[1,*], David R. Cooke[1,2], Lejun Zhang[1,2], Nathan Fox[1], and Jay Thompson[1]

[1]Centre for Ore Deposit and Earth Sciences (CODES), University of Tasmania, Private Bag 79, Hobart, Tasmania 7001, Australia
[2]Transforming the Mining Value Chain, an ARC Industrial Transformation Research Hub, University of Tasmania, Private Bag 79, Hobart 7001, Australia

Abstract

Distinctive quartz-rich unidirectional solidification textures (USTs) occur in apical carapaces of the Sn-mineralized Heemskirk Granite in western Tasmania (SE Australia). They are spatially associated with abundant tourmaline-filled orbicules and cavities that have been overprinted by widespread tourmaline-quartz veins. Multiple UST-quartz layers that are intercalated with aplitic layers, and can locally extend for hundreds of meters. Individual UST layers consist dominantly of hexagonal quartz (>95%) with minor K-feldspar, plagioclase, biotite, muscovite, and magnetite. Scanning electron microscope-cathodoluminescence (SEM-CL) reveals that the aplitic quartz is homogeneous and CL-bright with minor CL-dark patches. The bases of the UST quartz crystals are homogeneous and CL-bright with minor thin CL-dark fractures, whereas the trigonal apexes of the UST-quartz display CL-oscillatory growth zones. LA-ICP-MS analyses show that UST-quartz has lower Ti, Li, and Sn than aplitic quartz, but higher Al, Li, Na, K, Mn, Fe, Ge, Rb, and Cs concentrations. At a pressure of ca. 1.3 kbar, the Ti-in-quartz geothermometer yields temperatures of 545 ± 40 and 580 ± 20 °C for the UST and aplitic quartz, respectively. The UST-quartz has higher Al/Ti values of 5.8 to 32, and Ge/Ti values of 0.02 to 0.16, than quartz phenocrysts in aplite layers, which is consistent with crystallization from a highly evolved fluid. The O-isotopic compositions (+5.1 to +10.2‰) of UST and aplitic quartz are consistent with magmatic source circulated by minor meteoric and/or formation waters. Magnetite crystals in USTs have low Cr, V, Ni, Co, Cr, Sc, and high Ti, Al, Mn, Sn, Ga contents, and are overgrown by chlorite. These minerals are interpreted to have formed at UST-melt interface where hydrothermal fluids reacted with igneous minerals. The results show that the UST layers in the Heemskirk Granite precipitated from magmatic-hydrothermal aqueous fluid exsolved from granitic melt during emplacement into the shallow crust (6–10 km). Such UST layers are characteristics of mineralized intrusions, and therefore provide significant indications for mineral exploration.

Keywords: Unidirectional solidification textures, cathodoluminescence, quartz trace elements, magnetite, exsolved aqueous fluid, Sn-mineralized granite

Introduction

Unidirectional solidification textures (USTs) are defined morphologically as mineral crystals grown in one direction from a solid groundmass (Shannon et al. 1982). Three principal types of USTs were recognized by Shannon et al. (1982) at the Henderson porphyry Mo deposit, including crenulate layers composed mainly of quartz or alkali feldspar, dendritic layers consisting of branching or plumose quartz and feldspar crystals, and intergrowth layers in which quartz is intergrown with alkali feldspar. Crenulate quartz layers, also known as comb quartz layers, are common in porphyry intrusions associated with many types of magmatic-hydrothermal ore deposits (Shannon et al. 1982; Carten et al. 1988; Kirkham and Sinclair 1988; Lowenstern and Sinclair 1996; Kirwin and Seltmann 2002; Lickfold et al. 2003, 2007; Wilson et al. 2003; Harris et al. 2004; Breiter et al. 2005; Cannell et al. 2005).

Such comb-quartz UST layers have been described variously as ribbon rocks, ribbon banded structures, rhythmically banded textures, brain rocks, ptygmatic veins, wormy veins, and Willow Lake-type layering (Kirkham and Sinclair 1988; Lowenstern and Sinclair 1996). Quartz is predominant in the comb layers, which often contain minor amounts of other minerals, such as alkali feldspar, plagioclase, biotite, tourmaline, and fluorite, as well as sulfide minerals. Breiter et al. (2005) documented feldspar- and zinnwaldite-dominated UST layers within a highly fractionated, volatile-rich peraluminous granite associated with Sn, W, and rare metal mineralization from western Krušné Hory Mountains (Czech Republic). Harris et al. (2007) reported magnetite-bearing USTs from the Ridgeway porphyry Au-Cu deposit in New South Wales (Australia).

Comb-quartz USTs typically alternate with aplitic interlayers. Anhedral quartz crystallizes from the granitic roof or walls, with an irregular contact with the aplitic substrate. The elongated axes of the comb quartz crystals are generally perpendicular to the plane of the UST layers. Their basal, inward-directed terminations (apices) have hexagonal morphologies, which point to the direction of progressive crystallization (Shannon et al. 1982; Kirkham and Sinclair 1988). Comb-quartz USTs typically occur in the roof zones or less commonly in the walls of shallow, apical intrusions linked to Cu, Mo, Au, and W mineralization in a broad

* E-mail: wei.hong@utas.edu.au

variety of geological settings. The intrusions that host UST layers range from diorite, via monzonite, to granite in composition, and typically have porphyritic textures (Carten et al. 1988; Kirkham and Sinclair 1988; Lowenstern and Sinclair 1996; Lickfold et al. 2003; Wilson et al. 2003; Harris et al. 2004; Cannell et al. 2005).

Comb-quartz UST layers have been mistaken for quartz veins, pegmatite or stockscheider pods within granitic stocks (cf. Schmitz and Burt 1990). This suggests that USTs could have previously been underreported, due to the challenges associated with their recognition. There are several genetic models for USTs (e.g., Kirkham and Sinclair 1988; Lowenstern and Sinclair 1996), but overall data on fluid compositions, pressure, and temperature, are lacking for their formation. This study documents distinctive quartz-rich (+ feldspar + biotite ± magnetite ± tourmaline) USTs from the Heemskirk Granite from western Tasmania, which is genetically related to some of the richest and largest tin deposits, Ag-Pb-Zn veins, and carbonate replacement deposits in Australia (Seymour et al. 2007). Cathodoluminescence textures, trace-element analyses, and oxygen isotope values of quartz, together with trace-element analyses of magnetite from USTs are presented to constrain the origin of quartz-dominated USTs and their relation to mineralization.

Geological setting

Regional geological history

Tasmania is principally composed of two distinctive geological domains: the western and eastern terranes, which are bounded by the Tamar Fracture System (Fig. 1). The eastern terrane consists of an Ordovician to Lower Devonian marine quartzwacke turbidite apron (Mathinna Supergroup; Fig. 1) that has been intruded by abundant Paleozoic granitoids ranging in age from 405 to 375 Ma (Black et al. 2005; Corbett et al. 2014; Hong et al. 2017a).

In the western terrane, the oldest exposures are of the lower to middle Rocky Cape metasedimentary sequences with U-Pb ages of 1450 to 1330 Ma (Halpin et al. 2014; Fig. 1). Neoproterozoic shallow marine shelf sedimentary successions (e.g., Oonah Formation) are unconformably overlain by Neoproterozoic to Early Cambrian volcano-sedimentary sequences (Togari Group; Corbett et al. 2014; Fig. 1). A Cambrian arc-continent collision led to the emplacement of voluminous allochthonous blocks (Berry and Crawford 1988) and produced the Mt. Read volcanic rocks and associated volcanic-hosted massive sulfide deposits in northwestern Tasmania (Large 1992). Late Cambrian siliciclastic conglomerates were overlain by the Ordovician-Early Silurian carbonates, both unconformably overlain by Silurian to Early Devonian siliciclastics (Seymour et al. 2007; Corbett et al. 2014). The Proterozoic and Paleozoic metasedimentary rocks were intruded by a series of I- and S-type granites with U-Pb ages between 374 and 350 Ma (Fig. 1; Black et al. 2005; McClenaghan 2006; Hong et al. 2017a). These granites are moderately to highly fractionated, and some of them produced world-class Sn-W deposits (e.g., Renison Bell Sn, Mt Bischoff Sn, Kara W, and King Island W; Fig. 1; Hong et al. 2017a).

Heemskirk Granite

The Heemskirk Granite is on the western coast of Tasmania and has an exposure area over 140 km² (Fig. 2). It has steep in-

trusive contacts with the Neoproterozoic metasedimentary rocks of the Oonah Formation. This granite extends beneath the Zeehan and Dundas mineral fields, and gravity modeling shows that it connects with the Pine Hill and Granite Tor granites at a depth >2 km (Leaman and Richardson 2003). The Heemskirk Granite has been subdivided into a white and a red phase, mainly based on the distinctive color of K-feldspar in both units (Hajitaheri 1985; Fig. 2a). The White phase of the Heemskirk Granite is more than 500 m thick, extending from the western coastline to the eastern margin. The Red phase is a ~300 m thick sill that overlies the White phase granite and is confined to the eastern half of the exposed intrusion (Fig. 2b). The White and Red phases are mineralogically similar, consisting of quartz, K-feldspar, plagioclase, with minor biotite and tourmaline. Accessory minerals such as zircon, monazite, titanite, apatite, and fluorite occur in both granite phases. Hornblende and allanite are observed in the Red phase, and muscovite, garnet, and cassiterite occur in the White phase (Hajitaheri 1985; Hong et al. 2017b).

The Heemskirk Granite is genetically associated with abundant Sn-W-Fe skarn and/or greisen deposits, Ag-Pb-Zn veins, and carbonate replacement deposits, and an unusual hydrothermal Ni deposit (Both and Williams 1968; Seymour et al. 2007; Keays and Jowitt 2013; Hong et al. 2017b). Since 1876, more than 35 occurrences and deposits have been discovered within and around the Heemskirk Granite (Hajitaheri 1985; Fig. 2a). Significant Sn-W deposits include the Federation, Globe, Sweeneys, Colemans, and Tenth Legion in the southern part of the granite, and the Severn, Queen Hill, Montana, and Oonah in the Zeehan field on the eastern flank of the granite (Leaman and Richardson 2003). These Sn-W skarns and greisens are estimated to contain >0.13 Mt of Sn (Seymour et al. 2007; Hong et al. 2017b). Vein-type Ag-Pb-Zn deposits in the Zeehan field yielded >0.19 Mt Pb and 750 ton Ag between the 1880s and 1950s (Both and Williams 1968). The substantial Zn content of the ores was not extracted by the processing techniques at that time. The Avebury hydrothermal nickel deposit with a resource of 29.3 Mt at 0.9% Ni is located at the contact between the southern boundary of the granite and ultramafic-mafic rocks (Keays and Jowitt 2013).

Quartz-rich unidirectional solidification textures

Quartz-rich unidirectional solidification textures (USTs) occur in the roof zone and on the margins of the White and Red phases of the Heemskirk Granite. They are exposed spectacularly at Trial Harbor and Granville Harbor (Fig. 2a), and also crop out at Mt. Agnew and other locations within the batholith. These UST-quartz layers have an intimate spatial and temporal relationship with distinctive tourmaline-rich textural features, such as tourmaline patches, orbicules, miarolitic cavities, and veins in the Heemskirk Granite (Figs. 2b–2c; Hong et al. 2017b).

The USTs in the Heemskirk Granite are defined mostly by euhedral quartz crystals up to 5 cm in length. Individual quartz crystals are normally 0.2 to 30 mm in diameter, and are much coarser than quartz phenocrysts (normally ≤0.2 mm) in adjacent aplitic rocks. Some layers may have been misidentified as pegmatite or stockscheider (e.g., Schmitz and Burt 1990) because of their megacrystic grain size (Figs. 3a–3b). There is commonly more than one layer of comb quartz in outcrop, with each layer alternating with aplite (Fig. 3). In some cases, thick
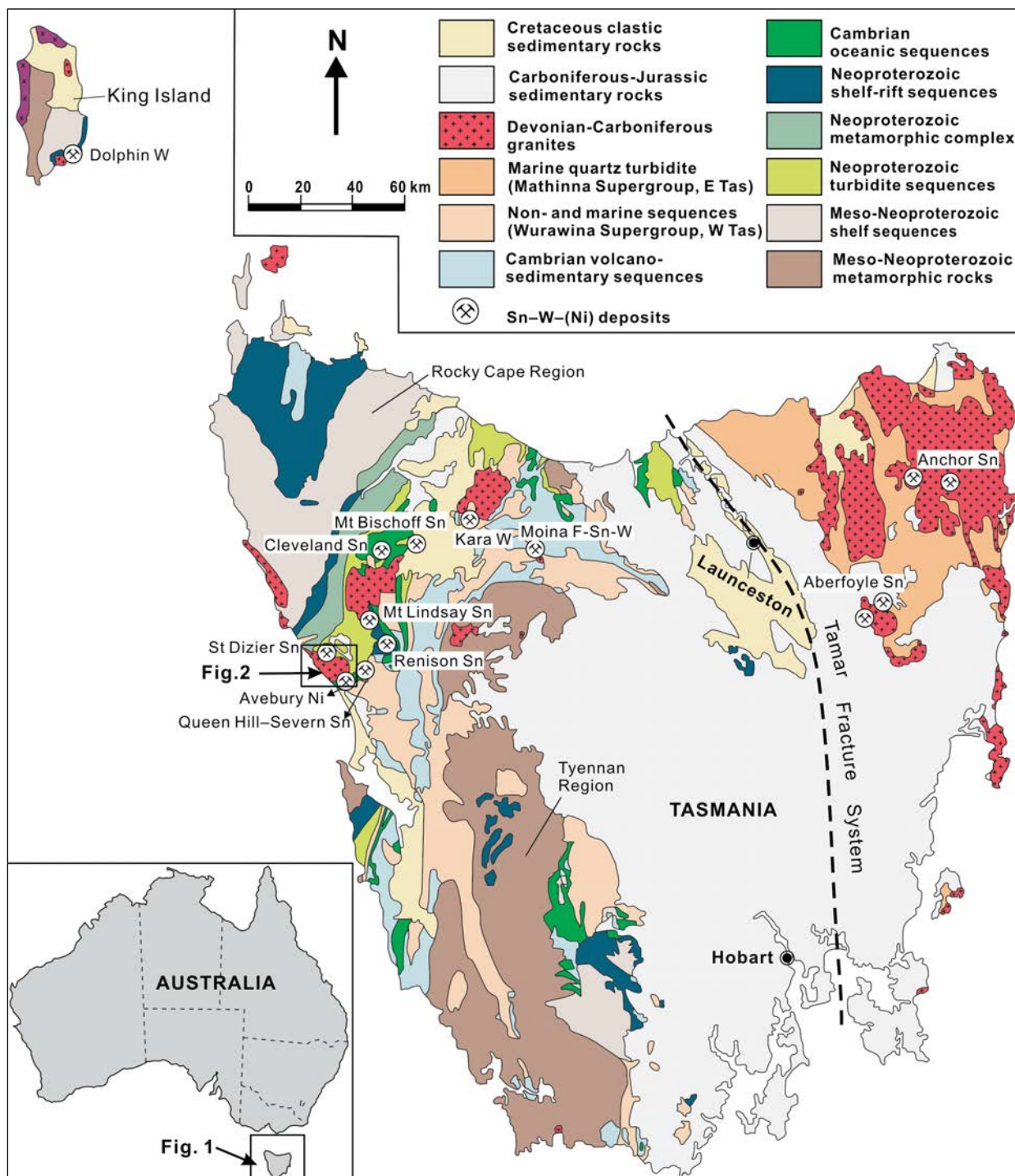
Figure 1. Simplified geological map of Tasmania and major Paleozoic granite-related Sn-W mineral deposits, SE Australia (modified from Seymour et al. 2007; Hong et al. 2017a). (Color online.)

quartz UST layers have locally bifurcated into two or more narrow UST-quartz bands (Fig. 3b). Comb quartz layers typically range in thickness from several millimeters to centimeters. They can extend along a strike continuously for more than tens of meters as subhorizontal bands (Fig. 3b), but more commonly occur as discontinuous, sinuous chains. Quartz layers are locally bent intensively, and some have been folded completely into a "necklace" style (Fig. 3c). Several 10 m long quartz layers locally disappear, and then re-emerge in nearby areas, and continue for another tens or hundreds of meters along strike.
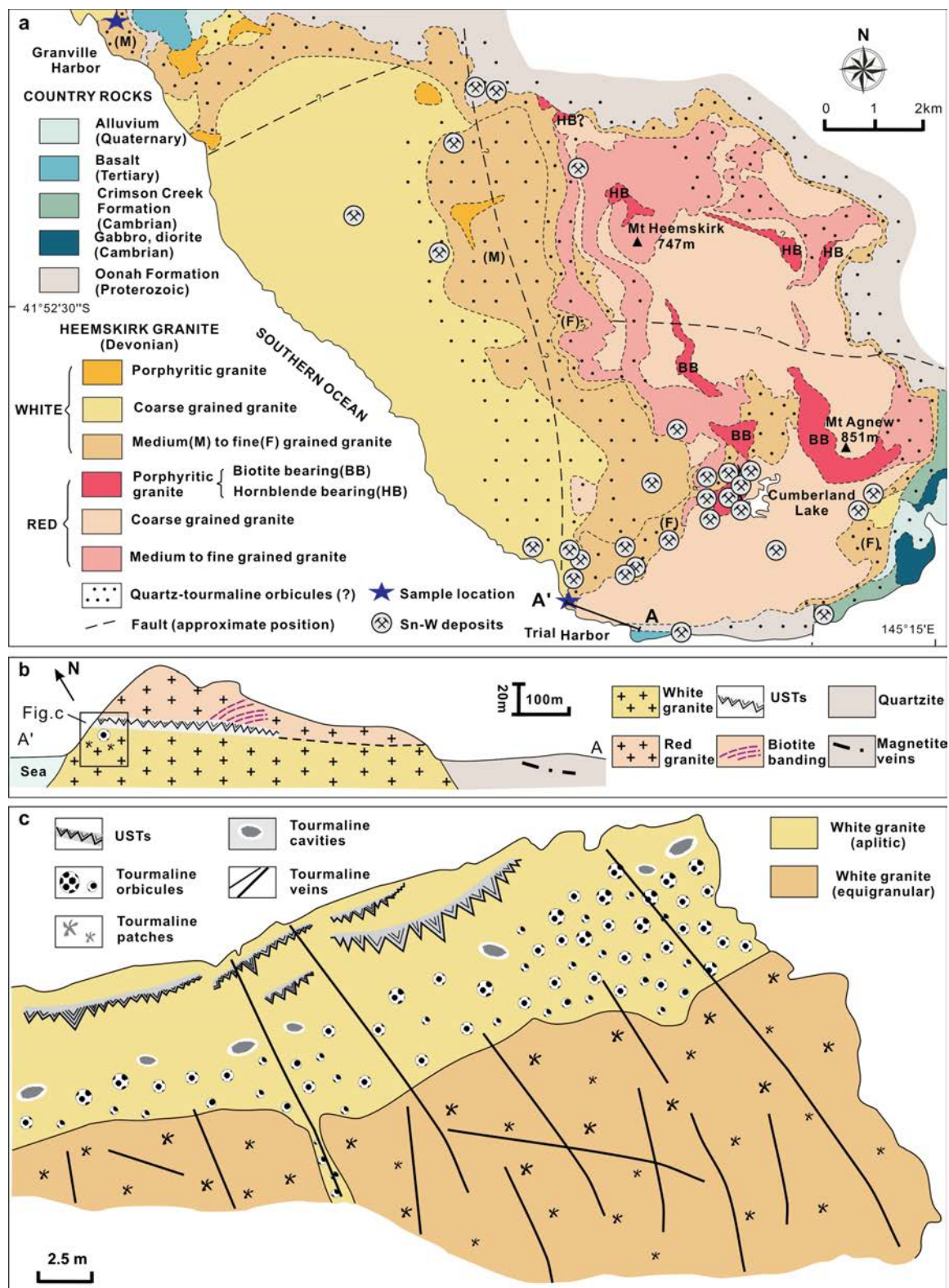
FIGURE 2. (a) Geological map showing the Heemskirk Granite and associated Sn-W deposits (after Hajitaheri 1985; Hong et al. 2017b). (b) Simplified cross-section A-A' is showing the outcrop at Trial Harbor of the Heemskirk Granite (Hong et al. 2017b). (c) Schematic cross section showing relative spatial distributions between UST-quartz layers and tourmaline-rich assemblages at Trial Harbor of the White Heemskirk Granite (Hong et al. 2017b). (Color online.)
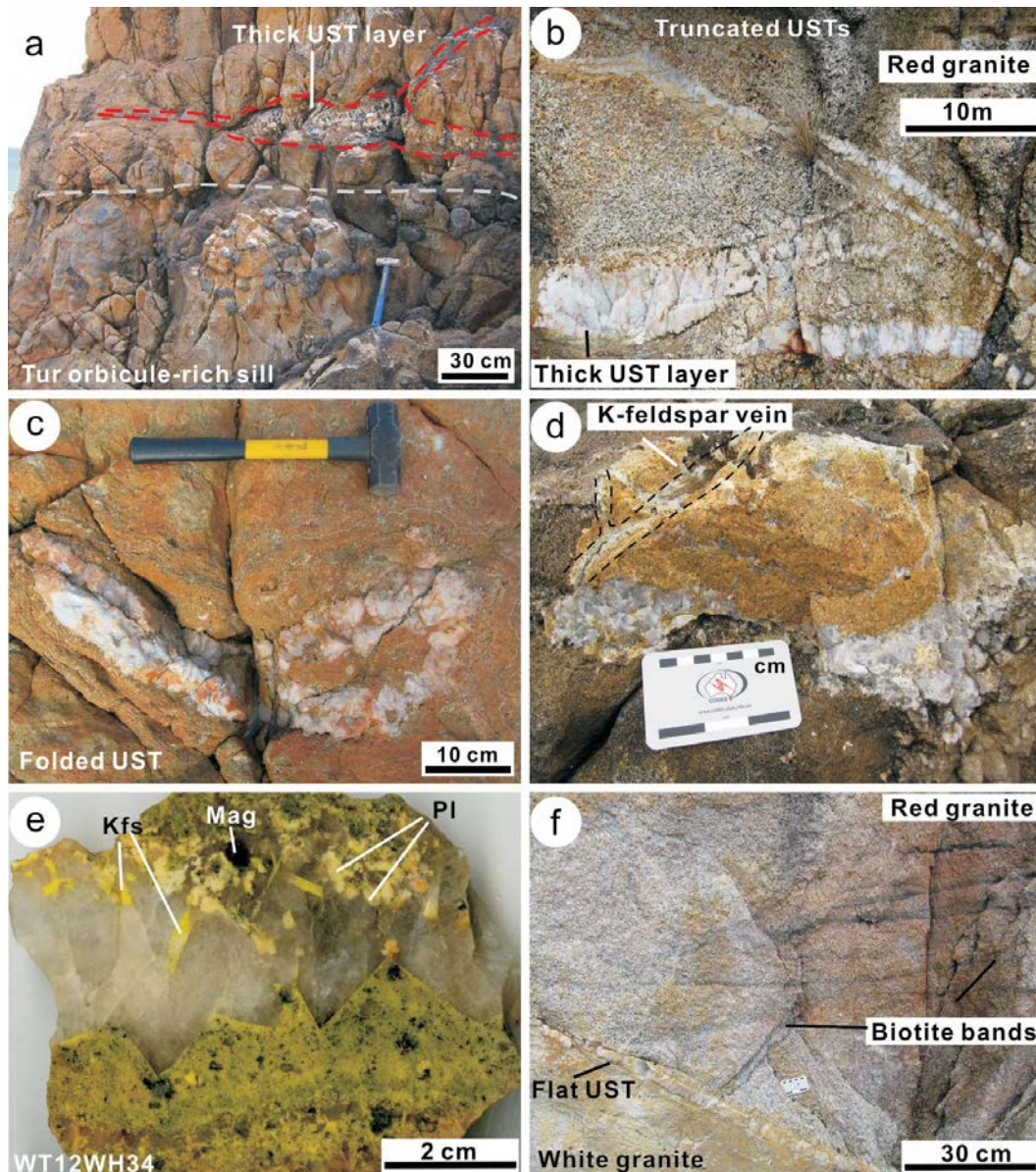
FIGURE 3. Photographs showing textural features of quartz-rich USTs in the Heemskirk Granite. (**a**) A thick UST layer consisting of quartz, feldspar, and minor tourmaline overlying the tourmaline orbicule-rich sill in the White granite at Trial Harbor. (**b**) Multiple UST-quartz layers at Trial Harbor, locally truncating and alternating with thin aplitic bands. (**c**) A folded quartz UST layer defining a "necklace" texture at Granville Harbor. (**d**) Multiple sinuous UST quartz layers are overprinted by K-feldspar veinlets at Trial Harbor. (**e**) Magnetite-bearing USTs (stained with cobalt nitrate) consisting of K-feldspar (yellow), plagioclase, quartz, and minor biotite from Granville Harbor. (**f**) A long, flat UST-quartz layer truncating biotite bands in the Red granite. Abbreviation: Kfs = K-feldspar, Mag = magnetite, Pl = plagioclase. Outcrop locations: (**a** and **d**) E145°09′23.93″, S 41°55′20.64″, elevation = 10 m; (**b** and **f**) E145°09′30.49″, S41°55′23.94″, elevation = 7.1 m; (**c** and **e**) E145°01′40.47″, S 41°48′34.80″, elevation = 1 m. (Color online.)

The long axes of quartz crystals are nearly perpendicular to the plane of each UST layer, and intervening aplitic layers (Figs. 3b, 3d, and 3e). Anhedral quartz crystallized on the base of the overlying aplite layer and grew downward into a volatile-rich pocket trapped below the aplite layers (e.g., Lowenstern and Sinclair 1996). The UST-quartz crystals have euhedral hexagonal terminations (Fig. 3e), whereas the alkali-feldspars exhibit nearly square morphologies, locally with identical cross-hatched

or sector twins (Fig. 4b). K-feldspar, plagioclase, and biotite are locally concentrated at the base of USTs (Fig. 4a), but they are much less abundant than quartz. From the base of UST layers, fine-grained alkali-feldspars project downward to the lower euhedral apical terminations (Fig. 4a). Trigonal K-feldspar crystals overgrown by anhedral quartz are defined by a cryptic, thin UST-layer dominated by K-feldspar (Fig. 4c), which formed prior to the main UST-quartz layer. These K-feldspar crystals

associated with UST quartz are commonly experienced a weak to intermediate muscovite alteration (Figs. 4a–4c). The downward-projecting apices of euhedral, coarse-grained quartz crystals have smooth contacts with the underlying aplite (Fig. 3e). However, petrographic observations reveal that the hexagonal quartz grains have been locally corroded and overgrown by very fine-grained quartz, feldspar, and biotite (Figs. 4e–4f). Quartz-feldspar over-

growths on the downward-pointing UST apices locally display granophyric textures (Fig. 4f), indicating that aplite crystallized rapidly after UST growth, probably due to undercooling (Kirkham and Sinclair 1988). Minor biotite is intergrown with K-feldspar below the individual undulating UST layers (Fig. 4a). Biotite also occurs as inclusions in coarse-grained quartz layers (Fig. 4d). Some USTs contain minor tourmaline (e.g.,
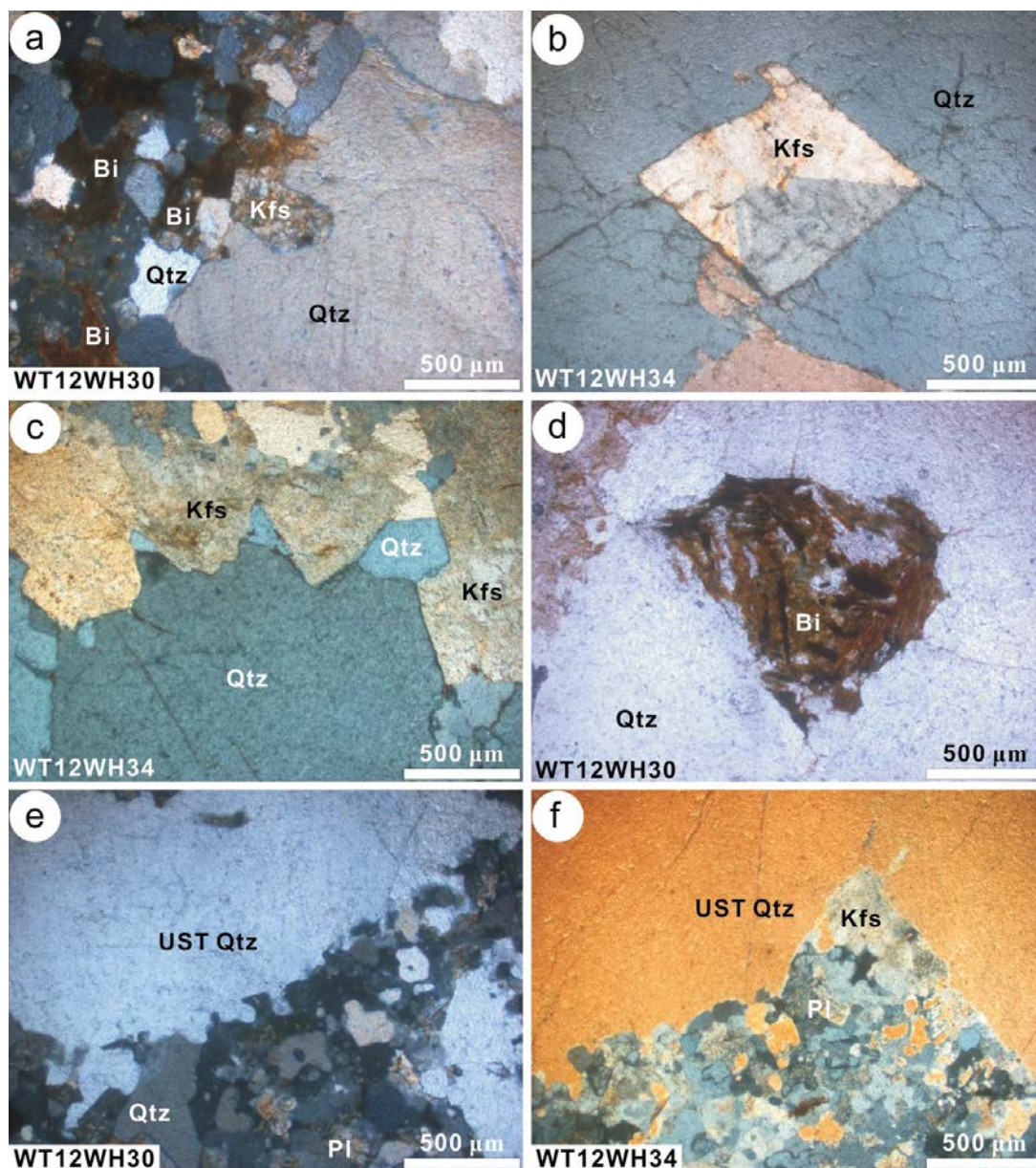

FIGURE 4. Photomicrographs showing textural features of USTs in the Heemskirk Granite. (**a**) On the bases of USTs, biotite, and K-feldspar are intergrown with coarse-grained quartz (Trial Harbor). (**b**) K-feldspar in coarse-grained quartz displaying roughly square morphologies and sector twins (Granville Harbor). (**c**) On the base of a UST, coarse-grained quartz is partly overgrown by a thin band of trigonal alkali-feldspar (Granville Harbor). (**d**) Irregular biotite occurs as inclusions in coarse-grained quartz. (**e** and **f**) The apex of a UST-quartz crystal has been corroded by mineral overgrowths, whereas quartz overgrowths in contiguous aplite locally exhibit granophyric textures. All photomicrographs were taken under cross-polarized light, except **d**, which was under plane-polarized light. Abbreviation: Bi = biotite, Kfs = K-feldspar, Mag = magnetite, Pl = plagioclase, Qtz = quartz. Sample locations: WT12WH30, E145°09′23.93″, S 41°55′20.64″, elevation = 20 m; WT12WH34, E145°01′40.47″, S 41°48′34.80″, elevation = 1 m. (Color online.)

Trial Harbor; Fig. 3a). On the northern margin of the granite batholith at Granville Harbor, adjacent to the contact with the carbonaceous Oonah Formation, the quartz-rich USTs locally contain a small amount of discrete magnetite grains (Fig. 3e). No sulfides have been observed in USTs within the Heemskirk Granite. Trace amounts of zircon, monazite, and rutile occur sparsely as isolated grains in quartz-dominated USTs.

The UST-bearing granitic sill is underlain by an aplitic sill enriched in tourmaline orbicules and miarolitic cavities in the apical region of the White Heemskirk Granite at Trial Harbor (Fig. 3a). Both sills overlie a domain enriched in tourmaline patches in the White granite (Hong et al. 2017b). Tourmaline-rich veins cut across UST-quart layers locally (Fig. 2c). K-feldspar (-muscovite) veinlets also locally crosscut the UST-quartz layer and extend into the overlying aplite (Fig. 3d). At Trial Harbor, a flat, quartz-rich UST layer points downward into the underlying White granite, extends continuously for a few tens of meters, and then is truncated by biotite-rich bands in the overlying Red granite (Figs. 2c and 3f). Hajitaheri (1985) originally documented the USTs at this contact as a quartz vein. This UST layer provides unambiguous evidence that the Red granite was intruded by the underlying White granite (cf. Shannon et al. 1982).

ANALYTICAL METHODS

SEM-CL and microprobe analysis

Quartz cathodoluminescence (CL) images were generated using a Cameca CL detector attached to an FEI Quanta 600 environmental scanning electron microscope (SEM) in the Central Science Laboratory (CSL) at the University of Tasmania (UTAS). Samples analyzed include quartz within USTs, quartz phenocrysts in aplite, and tourmaline-quartz veins from the Heemskirk Granite. A total of 30 carbon-coated, polished thick sections (200 μm) and mounts were CL-imaged at an accelerating voltage of 20 kV and beam current of ~3 nA.

Magnetite compositions were analyzed on a Cameca SX100 electron microprobe analyzer (EMPA) equipped with five tunable wavelength-dispersive spectrometers at the CSL. Elements analyzed include Fe, Si, Ti, Al, Ca, Al, Mg, V, Cr, Mn, K, Na, Cl, and F. Beam conditions for magnetite analyses were 15 kV accelerating voltage, 10 nA beam current, 10 μm beam diameter, and a 40° take-off angle. Elements were acquired using analyzing crystals LLIF for Cr, Mn, Fe, and V; LPET for P and Cl; PET for K, Ca, and Ti; TAP for Al, Mg, Na, and Si; and PC0 for F. Oxygen was calculated by cation stoichiometry. The Fe^{2+} and Fe^{3+} concentrations in magnetite were calculated using the formula of Droop (1987). Standards used for calibration were the following natural minerals: wollastonite (Ca, Si in magnetite), olivine (Mg in magnetite), magnetite (Fe in magnetite), rhodonite (Mn in magnetite), gahnite (Al and Zn in magnetite), tugtupite (Cl), and topaz (F). Counting times were 10 s for Na, Si, and Cl; 20 s for Mg, K, Al, Cr, Mn, Fe, and V; 30 s for Ca and P; 40 s for Ti; and 45 s for F. The detection limits at 3σ above mean background varied from 0.01 to 0.05 wt% for these components with 99% confidence.

LA-ICP-MS analyses

Trace elements of quartz and magnetite from the Heemskirk Granite were analyzed using a Resonetics Resolution S155 laser ablation system that utilizes a Coherent Compex Pro 110 ArF excimer laser operating at 193 nm wavelength and a 20 ns pulse width. The laser is coupled to an Agilent 7900cs quadrupole ICP-MS housed at CODES analytical laboratories, UTAS. All quartz samples were SEM-CL checked, and then they were ablated on 43 μm diameter spots using the laser at 10 Hz and an energy density of approximately 13.7 J/cm². The elements analyzed were Li^7, Na^{23}, Mg^{23}, Al^{27}, Si^{29}, K^{39}, Ca^{43}, Ti^{49}, V^{51}, Cr^{53}, Mn^{55}, Fe^{57}, Cu^{65}, Zn^{66}, Ge^{74}, As^{75}, Rb^{85}, Sr^{88}, Zr^{90}, Nb^{93}, Ag^{107}, Sn^{118}, Sb^{121}, Cs^{133}, Nd^{146}, Gd^{157}, Hf^{178}, Ta^{181}, Au^{197}, Pb^{208}, Bi^{209}, and U^{238}. Magnetite grains were measured on 34 μm diameter spots using the same laser system at 5 Hz and energy density 3.18 J/cm². Elements analyzed were Li^7, Na^{23}, Mg^{24}, Al^{27}, Si^{29}, K^{39}, Ca^{43}, Sc^{45}, Ti^{47}, V^{51}, Cr^{53}, Mn^{55}, Fe^{57}, Co^{59}, Ni^{60}, Cu^{65}, Zn^{66}, Ga^{69}, Ga^{71}, As^{75}, Sr^{88}, Y^{89}, Zr^{90}, Ag^{107}, Sn^{118}, Sb^{121}, Ce^{140}, Pb^{208}, Bi^{209}, and U^{238}.

For quartz analyses, the primary standard NIST612 was measured using a 64 μm spot size (10 Hz, 3.53 J/cm²). Pure silica glass, GSD-1g, and a quartz reference material from Audétat et al. (2015) were used as secondary external standards (47 μm, 10 Hz, 10.8 J/cm²; 3.53 J/cm² for GSD-1g), respectively. For magnetite, GSD-1g and BCR-2g were used as the primary (64 μm, 5 Hz, 3.18 J/cm²) and secondary standards (34 μm, 5 Hz, 3.18 J/cm²), respectively. Standard analyses were used to compare values for each given element, and to correct for differences in spot size between the primary standard and unknowns.

An Excel-spreadsheet laser template (CODES, unpublished) was used for data reduction. A theoretical Si value of 467 400 ppm along with Fe values obtained by EMPA were used as the internal standard elements for quartz and magnetite, respectively. The LA-ICP-MS spectral curves of quartz and magnetite were commonly chosen to start at 40 s and end at 85 s during data reduction. For those analyses in which solid or fluid inclusions were accidentally ablated, the anomalous spikes within the spectra were avoided during data processing. Quartz and magnetite results were normalized to the GSD-1g and BCR-2g glasses, respectively, measured in the same analytical session using GeoReM preferred values. A total of 125 quartz analyses and 32 magnetite analyses were retained after the rejection of any contaminated LA-ICP-MS spectra. Detection limits for most trace elements were in the range of 0.001 to 1 ppm (Supplementary[1] Material 1 and 2).

Oxygen isotope analyses

The oxygen isotopic compositions of quartz samples were measured using a CAMECA ims7f secondary ion mass spectrometer (SIMS) at the Department of Geological Sciences, University of Manitoba, Canada. Operating conditions and correction methods of instrumental mass fractionation and matrix effects were similar to those described by Fayek et al. (2002) for O-isotope analysis. A ~2 nA primary ion beam of Cs^+ accelerated at 10 kV was focused to a 15–20 μm spot size. The sample-accelerating voltage and electrostatic analyzer in the second column were set to –8.75 and –9 kV, respectively. The Balzers SEV 1217 electron detector has an overall dead time of 20 ns. A ±25 V energy window was setup with 250 V offset. The entrance slit was set at 247 μm with a mass resolving power of 347. Analyses of $^{18}O^-$ and $^{16}O^-$ were collected successively in ~10 min, which comprised 70 cycles with an eGun. The calculated precisions for individual spot reproducibility on the quartz standard were 0.1‰, 0.3‰, and 0.2‰ from January 7th to 9th (2014). All oxygen isotope data (δ^{18}O) are reported as‰ unit relative to Vienna-Standard Mean Ocean Water (V-SMOW).

ANALYTICAL RESULTS

SEM-CL textures of quartz

The CL textures of quartz phenocrysts in aplite layers are dominated by homogeneous bright luminescence with minor small CL-dark patches (<50 μm) and thin CL-dark healed fractures (Fig. 5a). In some aplitic quartz grains, CL-dark cobweb and patchy textures are well developed within CL-bright quartz (Fig. 5b). Some of the CL-dark patches are up to several hundred micrometers in diameter. These features contrast with the euhedral oscillatory zones of dark to bright CL intensity in the quartz grains from tourmaline veins of the Heemskirk Granite (Fig. 5c).

The bases of UST layers have jagged contacts with the host granites, and are characterized by homogeneous, CL-bright quartz. Thin (1–2 μm), CL-dark fractures cut the bright-CL quartz grains (e.g., Fig. 5d). Some thicker CL-dark cracks and patches (>10 μm), together with K-feldspar inclusions, are interstitial to CL-bright quartz crystal mosaics (see figure later in the section about oxygen isotopes). These features are similar to those in aplitic and granitic quartz grains in the Heemskirk Granite (cf. Figs. 5a–5b).

The bases and lower apices of individual quartz grains from USTs have contrasting SEM-CL textures (Figs. 5d and see figure later in the section about oxygen isotopes). The downward-projecting apices of quartz crystals in USTs have distinctive CL-gray to CL-bright bands that define euhedral oscillatory growth zones (Figs. 5d). The growth zones are characterized by
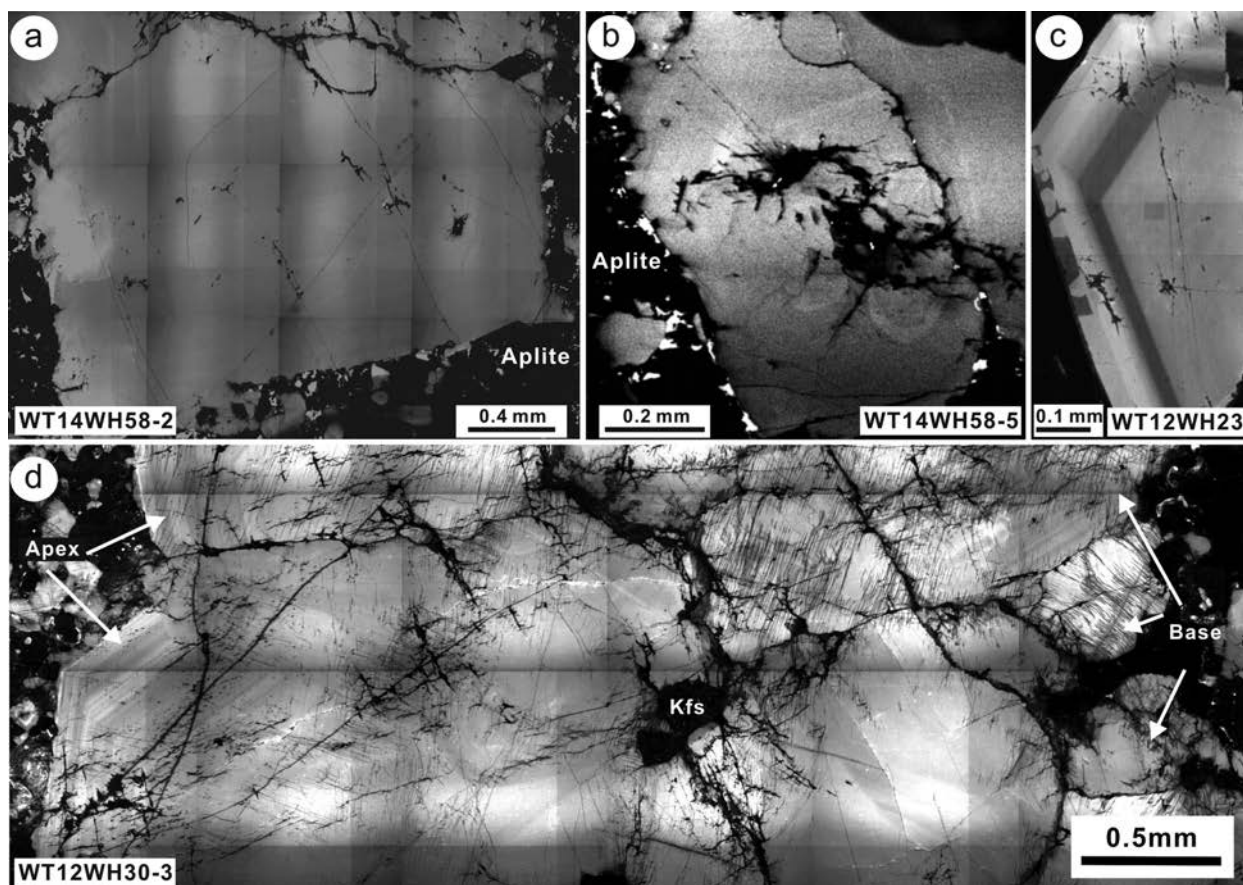
FIGURE 5. SEM-CL textures of aplitic quartz (**a–b**), quartz in tourmaline vein (**c**), and comb-layered UST quartz (**d**) from the Heemskirk Granite. Kfs = K-feldspar.

fine laminae (5 to 20 μm wide) that are parallel to grain edges, but only occur on the trigonal boundaries, and are restricted to domains that are several hundred micrometers thick (see figure later in the section about oxygen isotopes). Multiple sets of CL-dark to CL-gray fractures and anastomosing patches locally cut the euhedral oscillatory zones (see figure later in the section about oxygen isotope). The oscillatory growth zones are similar to those observed in quartz from tourmaline veins (cf. Fig. 5c).

Trace elemental and O-isotopic compositions of quartz

Trace-element concentrations. Analytical results for each spot of UST and aplite quartz are tabulated in Supplementary[1] Material 1A. The ranges and medians of trace-element concentrations in quartz from tourmaline-rich features and Pb-Zn sulfide veins are presented in Supplementary Material 1B. Most of the trace elements in aplitic and UST quartz have similar compositional ranges to those in tourmaline orbicules and cavities from the Heemskirk Granite, and contrast with those from quartz in tourmaline-rich veins (Supplemental[1] Table S1; Fig. 6). Aluminum concentrations in quartz from the aplitic layers of the Heemskirk Granite range from 186 to 704 ppm, with a median of 215 ppm (Fig. 6a), whereas Li has a range of 22.8 to 51.4 ppm (median = 31.7 ppm; Fig. 6b). Titanium in aplitic quartz has concentrations of 21.7 to 81.0 ppm, and Ge contents

fluctuate between 0.763 and 1.69 ppm (Supplemental[1] Table S1; Fig. 6c). Fe, Na, K, Mg, Zn, and Rb concentrations are mostly above their respective detection limits, with median values of 18.0, 3.58, 6.13, 1.49, 0.344, and 0.153 ppm (Supplemental[1] Table S1; Fig. 6).

Al, Li, Na, Mg, Ge, Zn, Sr, Pb, Rb, and Cs concentrations in UST quartz are consistently higher than those in aplitic quartz in the Heemskirk Granite (Supplemental[1] Table S1; Fig. 6). Aluminum in UST quartz ranges from 101 to 1196 ppm (median = 302 ppm), a broader range than in aplitic quartz (Fig. 6a). The ranges of Li concentrations mostly overlap between UST and aplitic quartz, but the median value is higher in UST quartz (39.6 ppm compared to 31.7 ppm: Fig. 6b). Titanium values in UST quartz mostly range from 11.0 to 68.0 ppm with a median of 26.7 ppm, which is lower than those in aplitic quartz (median = 40.5 ppm; Fig. 6c). The median Fe content in UST quartz (34.6 ppm) is almost as twice as high as in aplitic quartz (17.9 ppm), with the highest spot value of 1240 ppm Fe detected in the aplitic and UST quartz (Supplemental[1] Table S1). Germanium has similar concentrations in aplitic and UST quartz (0.763 to 1.72 ppm), but its median is higher in UST quartz (1.32 ppm; Fig. 6f). Tin concentrations mostly overlap between UST and aplitic quartz grains and are typically lower than 0.1 ppm, with medians of 0.090 and 0.061 ppm, respectively (Supplemental[1] Table S1; Fig. 6i).
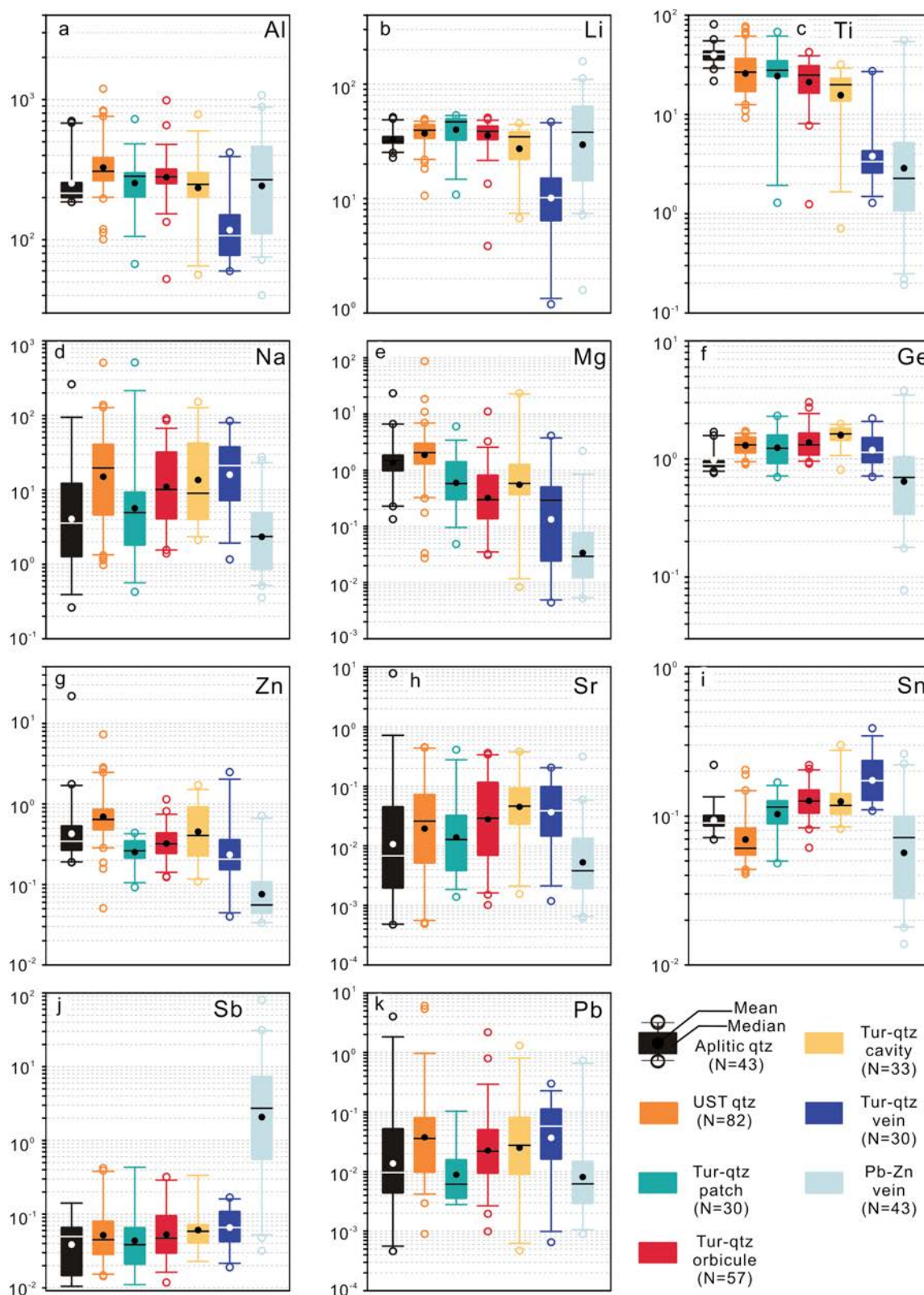
FIGURE 6. Percentile box and whisker plots showing the trace-element compositions of different quartz types from the Heemskirk Granite. (**a**) Al, (**b**) Li, (**c**) Ti, (**d**) Na, (**e**) Mg, (**f**) Ge, (**g**) Zn, (**h**) Sr, (**i**) Sn, (**j**) Sb, and (**k**) Pb. Tur = tourmaline, Qtz = quartz. Aplitic and UST quartz data from this study, other quartz data from Hong (2016). (Color online.)

Oxygen isotopes. Four oxygen isotopic analyses of aplitic quartz phenocrysts from the Heemskirk Granite (Trial Harbor), yielded a restricted range from +6.5 to +7.5‰ (Fig. 7; Supplemental[1] Table S2), with an average of +6.7‰. Two oxygen isotopic profiles were analyzed for UST-quartz crystals, with values from the base to the lower apex varying from +11.4 to +10.0‰ (average +10.8‰, n = 6) and from +7.2 to +8.6‰ (average +7.8‰, n = 6), respectively (Fig. 8). The $\delta^{18}O_{V-SMOW}$ values for UST-quartz are mostly higher than those of aplitic quartz (Fig. 7). The $\delta^{18}O_{V-SMOW}$ compositions of fluids in equilibrium with quartz were calculated using the equation from Clayton et al. (1972), with temperatures determined by the Ti-in-quartz geothermometer (Huang and Audétat 2012; Supplemental[1] Table S2).

Trace element and isotopic profiles of UST quartz. Figure 8 comprises the oxygen isotopic and trace-element profiles of two coarse-grained UST-quartz crystals from the Heemskirk Granite. Both of the UST-quartz grains have CL-bright intensity at their bases and euhedral oscillatory CL-zones at their lower apices (Figs. 8a–8b). Monovalent cations in UST-quartz, such as K^+ and Rb^+, decrease systematically from the base to the lower apex of each crystal, whereas Li^+, Na^+, and Cs^+ remain mostly unchanged (Figs. 8a–8b). Divalent cations, including Mg^{2+}, Zn^{2+}, and Mn^{2+}, do not display any consistent compositional variations across the UST-quartz crystals (Fig. 8).

Most of the trivalent (Al^{3+}, Fe^{3+}) and tetravalent cations (Ti^{4+}) in the UST-quartz are enriched in the CL-bright bases compared to the oscillatory CL-zoned lower apices (Fig. 8). Based on the Ti-in-quartz geothermometer from Huang and Audétat (2012), the two UST quartz crystals have temperatures ranging from 650 to 550 °C (Fig. 8). The calculated temperatures decrease from the base to the apex domains in an individual UST-quartz, consistent with the Ti, Al, Fe, K, and Rb concentration patterns (Fig. 8). Increases in the Al, K, and Rb contents from the base to the apex of each crystal are likely to result from contamination of micro- and nano-scale fluid inclusions (cf. Götze et al. 2004), although Na concentrations do not change much across the quartz grains (Fig. 8). In situ SIMS analyses show that CL-dark patches and fractures in CL-bright quartz have lower O-isotope compositions (Fig. 8).

Textures and compositions of magnetite

Anhedral magnetite grains are disseminated in some coarse-grained UST quartz layers in the Heemskirk Granite at Granville Harbor (Fig. 3e). Magnetite grains are typically less than 1 cm in diameter, but locally can be up to several centimeters (Fig. 9a). The magnetite occurs in the bases of individual UST layers, where it is intergrown with alkali-feldspar, plagioclase, and biotite (Figs. 3e and 9a). The alkali-feldspar crystals have been partly replaced by muscovite, whereas the magnetite grains are generally rimed by chlorite (Fig. 9b). Relict biotite cores (<0.25 cm in diameter) are present in the chlorite rims (Fig. 9b), which suggests that chlorite replaced magnetite and biotite. Magnetite is locally common as an accessory mineral in the aplite phase at Granville Harbor but has not been observed at Trial Harbor. The fractured magnetite in the aplite at Granville Harbor is commonly filled and overgrown by chlorite (Fig. 9c), a similar texture to the magnetite in the UST quartz
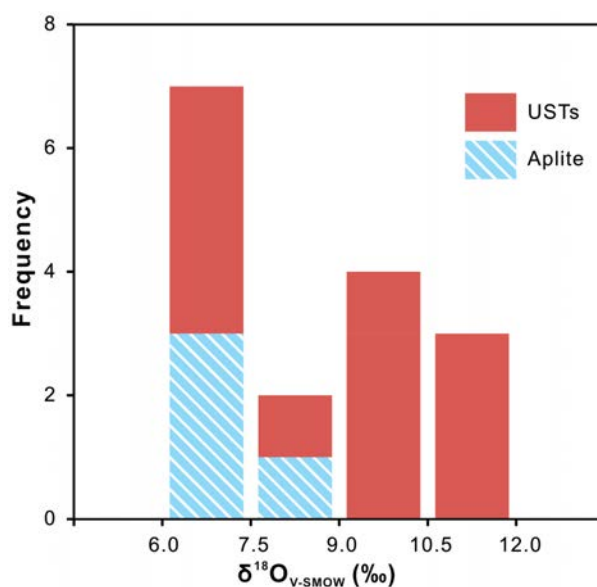
(Fig. 9b). BSE images of magnetite from UST and aplite layers lack compositional zoning (Figs. 9b and 9c).

The maximum, minimum, and mean values of major, minor, and trace elements in magnetite are summarized in Supplemental[1] Table S3. Iron contents in magnetite range from 58.7 to 71.9 wt% with an average value of 66.5 wt% (Supplementary[1] Material 2A), which is significantly lower than stoichiometric magnetite (~72.4 wt%). The Al_2O_3 and TiO_2 contents in magnetite have similar ranges between 0.6 and 9.5 wt% and average values of ~2.3 wt% (Supplemental[1] Table S3). SiO_2 concentrations in all analyzed magnetite have an average value of 0.62 wt%, locally up to 4.78 wt% (Supplemental[1] Table S3). The magnetite grains from UST samples have higher Al_2O_3, TiO_2, and SiO_2 contents than those from the aplite (Supplemental[1] Table S3). Other elements in magnetite, including CaO, V_2O_3, K_2O, Na_2O, MgO, MnO, P_2O_5, and Cr_2O_3 are typically below 0.05 wt% (Supplemental[1] Table S3).

LA-ICP-MS analyses show that the Mn, Mg, Zn, and Ga concentrations in magnetite are high ranging from hundreds of thousands of parts per million. Other trace elements such as As, Sn, and Pb range from tens to hundreds of parts per million, whereas Sc, V, Co, Cu, Li, Zr, and U typically average tens of parts per million, and Ni, Cr, Sr, Sb, Ce, Bi, and Ag are mostly below 10 ppm, or below detection limits (Supplemental[1] Table S3; Supplemental[1] Material 2B). Some Na, K, and Ca concentrations range up to hundreds to thousands of parts per million, but about 50% of the analyses are below their detection limits. In general, magnetite grains from the USTs have higher Li, Mg, Na, K, Mn, Zn, Cu, Sc, Co, As, and Bi concentrations than magnetite grains from the aplite (Supplemental[1] Table 3). Sn and Ga concentrations are enriched in magnetite from the aplite relative to the UST samples, whereas both magnetite types have similar concentration ranges and average values V, Cr, Co, Y, Zr, Ce, Pb, U, and Sb (Supplemental[1] Table S3).
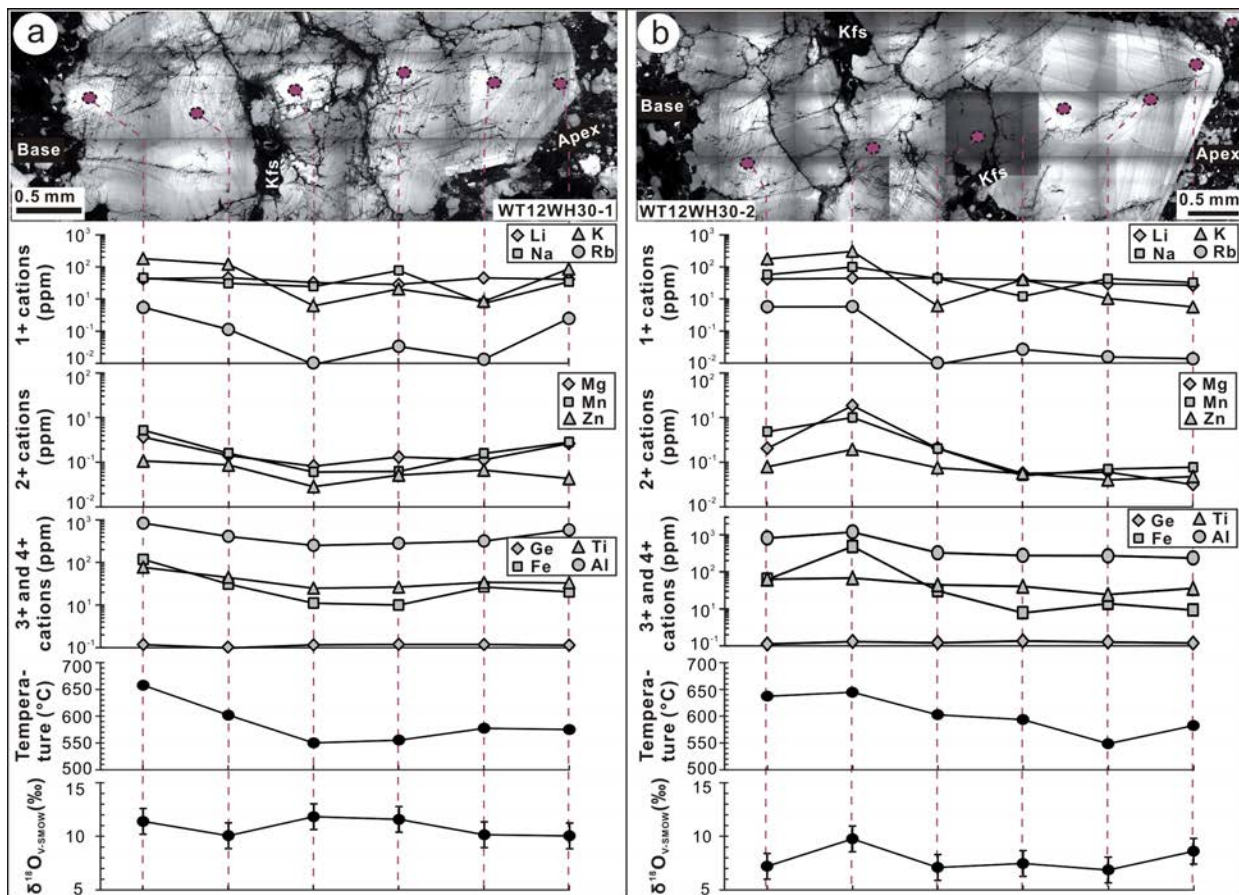
FIGURE 8. Combined SEM-CL, LA-ICP-MS and SIMS profiles showing textural, elemental, and O-isotopic variations across UST-quartz grains. (**a**) Sample WT12WH30-1, (**b**) Sample WT12WH30-2. Kfs = K-feldspar. (Color online.)

DISCUSSION

Quartz chemistry implications

Fluid sources. Trace-element contents of quartz from the aplitic layers overlap mostly with those of quartz intergrown with patchy tourmaline (+ K-feldspar + biotite) in the Heemskirk Granite (Figs. 6, 10, and 11). The two types of quartz display similar CL textures, characterized by bright-CL domains cut by CL-dark patches and cracks (Figs. 5a and 5b; Hong 2016). The calculated $\delta^{18}O_{V-SMOW}$ composition of fluids in equilibrium with aplitic quartz (average = +5.4‰ at temperature 600 °C; Supplemental[1] Table S2) are lower than the whole-rock $\delta^{18}O$ values of the Heemskirk Granite (+10‰; Hajitaheri 1985), and are close to the lower end-member of $\delta^{18}O$ values for granitic rocks worldwide (+6 to +10‰; Hoefs 2009). It is possible that small volumes of low $\delta^{18}O_{V-SMOW}$ fluids (e.g., meteoric and/or formation waters; Taylor 1974) were circulated into the granitic melts from which aplitic quartz phenocrysts precipitated. Quartz in the aplitic layers is concluded to have a magmatic origin, despite the slightly low $\delta^{18}O_{V-SMOW}$ values.

Euhedral UST-quartz grains in the Heemskirk Granite have trace-element compositions comparable to those of comb quartz in USTs reported by Lowenstern and Sinclair (1996).

The Heemskirk Granite UST-quartz crystals are characterized by higher abundances of Al, Li, Na, Mg, Fe, Mn, Ge, Zn, Sr, Pb, Rb, and Cs than the aplitic quartz (Supplemental[1] Table S1; Fig. 6). They have similar compositional ranges to those in quartz from tourmaline-filled orbicules and cavities (Figs. 6, 10, and 11). The calculated $\delta^{18}O_{V-SMOW}$ values of fluids in equilibrium with the WT12WH030-2-1 UST quartz (average = +9.3‰) are higher than those of the WT12WH030-2-2 UST quartz (average = +6.3‰) and aplitic quartz (average = +5.4‰), implying the former UST quartz crystallized from a magmatic fluid ($\delta^{18}O$ = +10‰) with lesser mixing of meteoric and/or formation waters (cf. Taylor 1974). Overall, the $\delta^{18}O_{V-SMOW}$ compositions of fluids in equilibrium with the UST quartz range from +5.7 to +10.2‰ with an average of +7.8‰ (n = 12; Supplemental[1] Table S2), consistent with a magmatic-hydrothermal fluid (cf. Hedenquist and Lowenstern 1994).

Sub-grain mineral and fluid inclusions. Aluminum is typically the most abundant trace element (up to thousands of parts per million) in quartz crystals from igneous rocks (Götze et al. 2004; Larsen et al. 2004; Rusk et al. 2008; Müller et al. 2010; Breiter et al. 2013; Tanner et al. 2013; Audétat et al. 2015; Drivenes et al. 2016). This is true of all quartz types from the Heemskirk Granite (Supplemental[1] Table S1; Figs. 6 and 10).
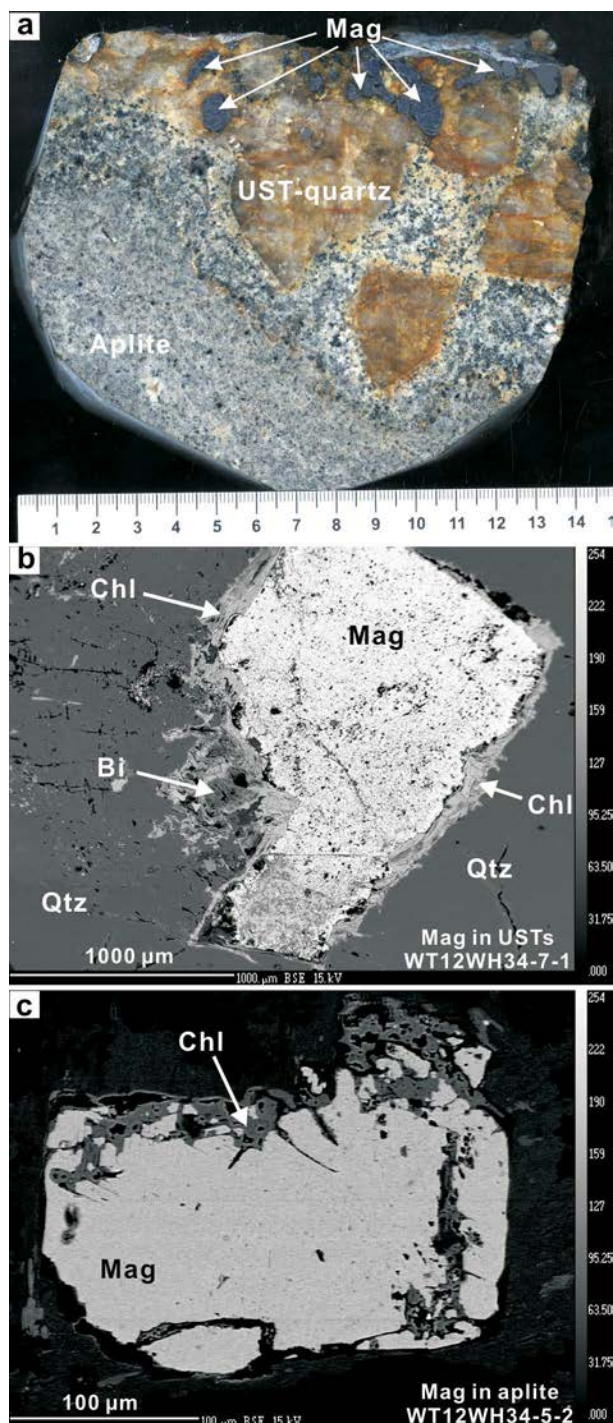
FIGURE 9. (**a**) Coarse-grained magnetite associated with UST-quartz in the Heemskirk Granite at Granville Harbor. BSE images showing textures of magnetite grains from the UST-layers (**b**) and aplite (**c**). Bi = biotite, Chl = chlorite, Mag = magnetite, Qtz = quartz. (Color online.)

Trivalent Al and monovalent ions (e.g., H^+, Li^+, Na^+, K^+, Rb^+, and Cs^+) can substitute for Si^{4+} in quartz lattice (Götze et al. 2004; Larsen et al. 2004). Although the atomic Al:Li ratios of the UST- and aplitic quartz deviate from the 1:1 line (Fig. 10a), Al

concentrations correlate positively with Li concentrations, suggesting a coupled $[Al^{3+}O_4Li][Si^{4+}]_{-1}$ element exchange vector for the growth of UST- and aplitic quartz (cf. Götze et al. 2004). Some K and Rb concentrations also correlate positively with Al contents in the quartz samples (Figs. 10b and 10c), which also presents the occurrence of element exchange vectors such as $[Al^{3+}O_4K][Si^{4+}]_{-1}$ and $[Al^{3+}O_4Rb][Si^{4+}]_{-1}$ (cf. Larsen et al. 2004).

The anomalously high K (>50 ppm) and Rb (>1 ppm) that increase systematically with Al in our quartz samples (Figs. 10b and 10c) most likely result from ablation of sub-grain K-feldspar and/or muscovite mineral inclusions and fluid inclusions (micro- to nano-scale) hosted in the UST- and aplitic quartz (Götze et al. 2004; Rusk et al. 2011). The UST and aplitic quartz locally contain small inclusions of K-feldspar that have undergone weak muscovite alteration (e.g., Fig. 3e). Fe and Mn generally have higher concentrations in UST quartz than in other quartz types, particularly one or two orders of magnitude higher than the hydrothermal vein quartz (Figs. 11a and 11b). These results are also interpreted to have been led by contamination of Fe-Mn-rich, micro- to nano-scale mineral and/or fluid inclusions (cf. Götze et al. 2004; Rusk et al. 2011), as the UST quartz crystals locally contain primary magnetite inclusions (Figs. 9a).

SEM-CL images have revealed internal textures and different generations of quartz crystals (Fig. 5), and then we avoided LA-ICP-MS analyzing the aplitic and UST quartz domains containing visible mineral inclusions related to fluid overprinting and hydrothermal alteration. Anomalous elemental spikes within LA-ICP-MS spectra were also discarded during quartz data processing. Some of our high Al, K, Rb, Na, Fe, and Mn concentrations detected in UST and aplitic quartz (Figs. 10 and 11) come from samples with homogeneous LA-ICP-MS spectra. Irrespective as to whether they are elevated due to contaminations by inclusions, the high Na, K, Rb, Fe, and Mn concentrations in the UST quartz show that the hydrothermal fluid was enriched in these elements relative to those of other quartz types.

Pressure-temperature estimation. Several recent studies in synthetic and natural quartz (Wark and Watson 2006; Ostapenko et al. 2007; Rusk et al. 2008; Müller et al. 2010; Thomas et al. 2010; Huang and Audétat 2012; Tanner et al. 2013) have illustrated that Ti concentrations in quartz correlate positively with temperature, and also are significantly controlled by pressure and TiO_2 activity (i.e., the TitaniQ thermometer). The TitaniQ thermometer proposed by Wark and Watson (2006) and Thomas et al. (2010) is applicable to quartz formed at high temperature (>600 °C), but appears to overestimate pressure and/or temperature for quartz precipitated in hydrothermal environments. Huang and Audétat (2012) therefore calibrated the Ti-in-quartz thermobarometer for hydrothermal quartz grown at variable growth rates (≤600 °C).

As trace amounts of isolated rutile crystals are detected within the UST quartz by SEM-EDS, the TiO_2 activity is estimated to be 1 for the quartz-forming fluid at Heemskirk (cf. Wark and Watson 2006). Our study detected lower Ti concentrations in the UST-quartz than the aplitic quartz (Fig. 10d), indicating that euhedral comb quartz precipitation occurred at lower temperatures under comparable pressures (e.g., Rusk et al. 2008; Müller et al. 2010; Tanner et al. 2013; Audétat et al. 2015). According to the Ti-in-quartz geothermometer of Huang and Audétat (2012), the UST- and aplitic quartz in the Heemskirk Granite are estimated
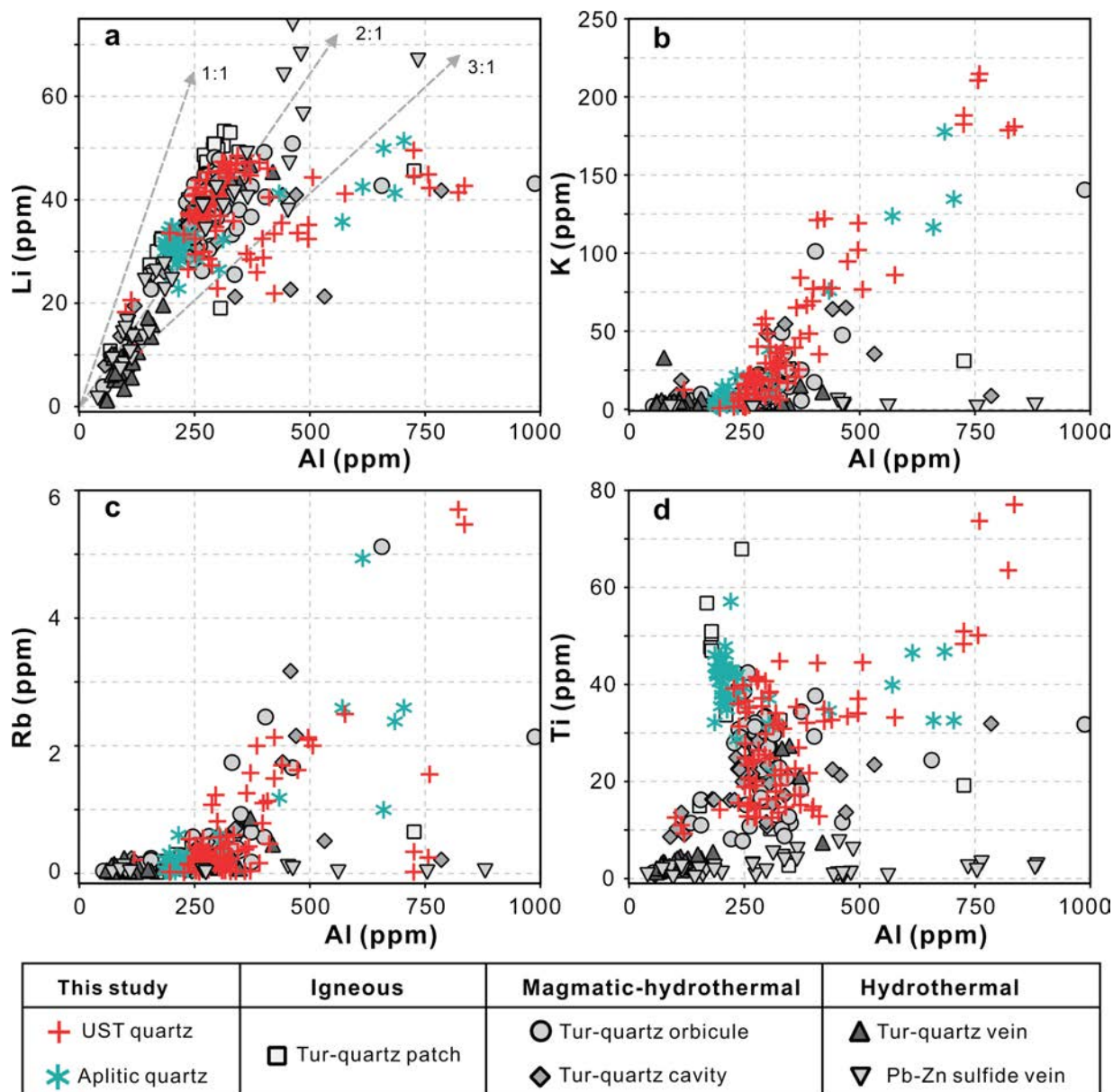
FIGURE 10. Trace-element plots showing chemical variations between aplitic quartz, UST-quartz and quartz from tourmaline-rich assemblages in the Heemskirk Granite. Al vs. Li (**a**), K (**b**), Rb (**c**), and Ti (**d**). Tur = tourmaline. Aplitic and UST quartz data from this study, other quartz data from Hong (2016). (Color online.)

to have formed at temperatures of 545 ± 40 and 580 ± 20 °C, respectively, assuming that they crystallized at a lithostatic pressure of ~1.3 kbar (Hajitaheri 1985; Hong 2016). The temperature range of UST-quartz in this study is consistent with those of the UST-quartz in the Au-Cu mineralized Northparkes porphyries (500–550 °C based on fluid inclusion microthermometry; Lickfold et al. 2003) and Ridgeway porphyries of New South Wales (average = 600 °C based on quartz-magnetite oxygen isotopic pairs; Harris et al. 2007).

Influence of crystal fractionation. Al/Ti and Ge/Ti ratios in quartz have been used as a petrogenetic indicator for the extent of crystal fractionation in felsic melt systems (Larsen

et al. 2004; Breiter et al. 2013; Drivenes et al. 2016). This is because Al and Ge typically behave incompatibly in quartz (Larsen et al. 2004), and Ti behaves independently of other trace elements (Thomas et al. 2010; Huang and Audétat 2012). Figure 11 shows plots of Al/Ti against Fe, Mn, Ge, and Ge/Ti for quartz from the Heemskirk Granite, highlighting significant variations between the aplite, USTs, and tourmaline-rich assemblages (Fig. 11). The Al/Ti vs. Ge/Ti plot best highlights the chemical differences in these various quartz types, as Al/Ti correlates positively with Ge/Ti from the high-temperature aplitic quartz, through UST quartz, to the low-temperature Pb-Zn sulfide-bearing quartz (Fig. 11d).
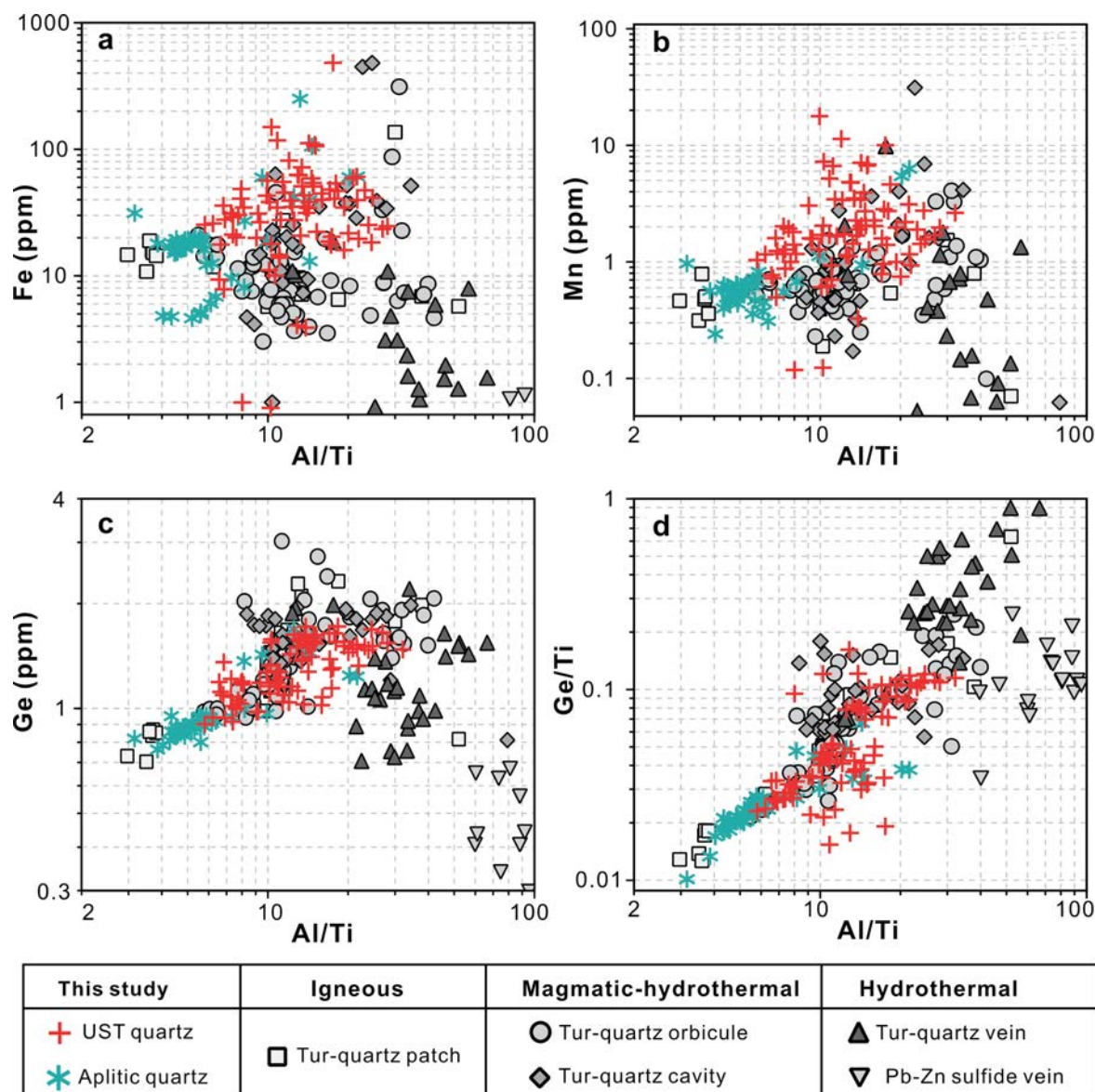
FIGURE 11. Plots of Al/Ti vs. Fe (**a**), Mn (**b**), Ge (**c**), and Ge/Ti (**d**) in quartz showing chemical variations between UST quartz and quartz from tourmaline-rich assemblages in the Heemskirk Granite. Tur = tourmaline. Aplitic and UST quartz data from this study, other quartz data from Hong (2016). (Color online.)

The ranges of Al/Ti and Ge/Ti ratios in aplitic quartz of the White Heemskirk Granite mostly overlap with those from the fine-grained S-type granites of SE Bohemia (Czech) and SW England (Breiter et al. 2013; Drivenes et al. 2016). This indicates that the White Heemskirk Granite has undergone high degrees of crystal fractionation, consistent with whole-rock compositions (Breiter et al. 2013; Drivenes et al. 2016; Hong et al. 2017a). The Al/Ti and Ge/Ti ratios for UST quartz are approximately one order of magnitude higher than those of aplitic quartz of the Heemskirk Granite (Fig. 11d), which implies that the USTs quartz precipitated are compositionally more evolved than those for the aplitic quartz (cf. Breiter et al. 2013; Drivenes et al. 2016).

Magnetite chemistry implication

Magnetite grains from both the USTs and aplite in the White Heemskirk Granite have similar textures, and their trace-element contents are similar (Figs. 8b, 8c, and 12; Supplemental[1] Table S3). It is unusual for this reduced S-type granite (Black et al. 2010; Hong et al. 2017a) to contain magnetite grains (Figs. 3e and 8). Reduced granites (mostly S-type) are classified as "ilmenite series," and commonly contain minor ilmenite with only rare magnetite (Ishihara 1977; Chappell and White 2001). Our study was revealed that the Heemskirk magnetite crystals have unique trace-element signatures compared to magnetite from other igneous rocks and mineral deposits (Fig. 12; Dupuis and Beaudoin 2011; Dare et al. 2014; Nadoll et al. 2014, 2015).
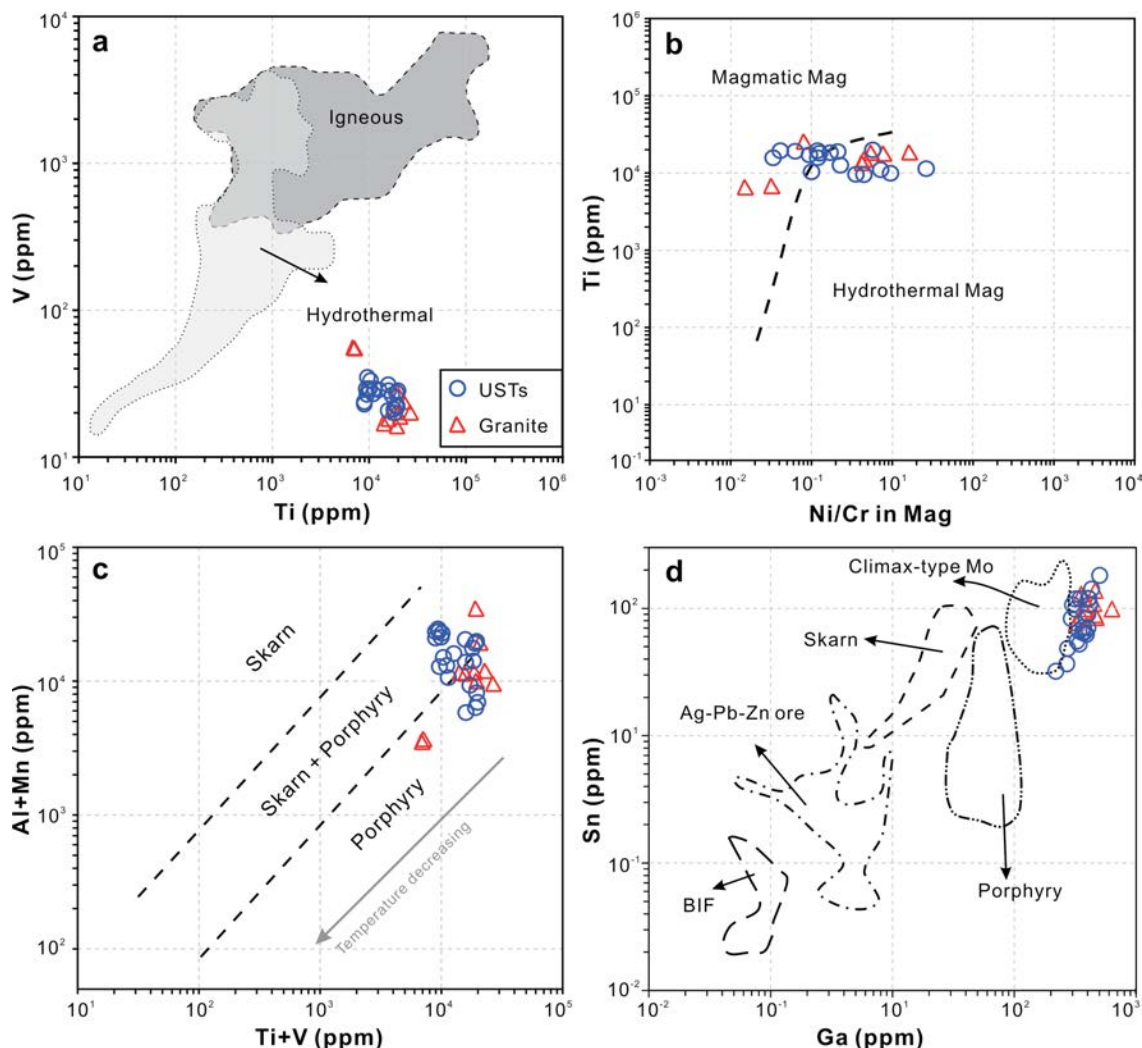
Figure 12. Plots showing trace elements in magnetite from the Heemskirk Granite. (**a**) Ti vs. V, (**b**) Ni/Cr vs. Ti, (**c**) (Ti+V) vs. (Al+Mn), (**d**) Ga vs. Sn. Original data fields in **a** and **c** from Nadoll et al. (2015), (**b**) from Dare et al. (2014), (**d**) from Nadoll et al. (2014). Mag = magnetite. (Color online.)

The V concentrations (26.9 ppm) of magnetite in the Heemskirk Granite (Fig. 12a) overlap with the low-temperature hydrothermal magnetite from porphyry and skarn Cu deposits reported by Nadoll et al. (2015), but are two orders of magnitude lower than magnetite from igneous rocks (including granitic intrusions) typically with V concentrations >1000 ppm (Nadoll et al. 2015). Furthermore, the Heemskirk magnetite crystals have Ti and Ni/Cr contents (Fig. 12b) that mostly overlap with the fields defined for hydrothermal magnetite from Dare et al. (2014).

Trace-element concentrations in magnetite, including Al, Mn, Ti, and V, correlate positively with the temperatures at which they may have precipitated (Dupuis and Beaudoin 2011; Nadoll et al. 2015). The Ti+V vs. Al+Mn plot (Fig. 12c) implies that the Heemskirk magnetite crystallized at temperatures similar to those for early-stage magnetite from hydrothermal porphyry Cu and skarn deposits (Nadoll et al. 2015). The Heemskirk magnetites at Granville Harbor have Sn (mean = 91.6 ppm) and Ga (mean = 378 ppm) concentrations that partly overlap with magnetite from

Climax-type Mo deposits and higher than magnetite from skarn and porphyry Cu deposits (Fig. 12d; Nadoll et al. 2014), probably implying that they formed at high-temperature conditions. These trace-element characteristics indicate that the Heemskirk magnetites within the USTs and aplite are hydrothermal in origin, as they are compositionally distinct from typical magmatic magnetite (Dare et al. 2014).

UST formation

The quartz-rich and magnetite-bearing USTs in the Heemskirk Granite are interpreted to have precipitated from an aqueous fluid exsolved from silicic magmas (e.g., Kirkham and Sinclair 1988; Lowenstern and Sinclair 1996; Fig. 13). Aqueous fluid phase separated from the crystallizing silicic magma during emplacement in the shallow crust (Fig. 13a; ca. 6–10 km; Burnham 1979). Continuous decompression during crystallization of the hydrous magmas gave rise to a spanning cluster of aqueous fluid bubbles (Candela 1991, 1997), which buoyantly ascended and

accumulated at the apex of the magma chamber where initial comb-quartz layers precipitated below the roof of the magma chamber (Fig. 13b). As the magma crystallized progressively, a large amount of fluid was concentrated within cupolas, especially in the roof zone. When fluid pressure exceeded the lithostatic load and tensile stress, the carapace underwent brittle fracturing (Burnham 1979), resulting in the release of fluid into adjacent wall rocks (Fig. 13c). Microscopic CL-dark healed fractures and associated K-feldspar-muscovite alterations (e.g., Fig. 3d) in euhedral comb quartz in the Heemskirk Granite may record

such brittle fracturing and fluid release. The volatile-rich aqueous fluid exsolved from the granitic melt was locally enriched in Fe, possibly partly related to overprinting on the pre-existing minerals (e.g., biotite) and/or partly due to incorporation of the Fe contents from the metasedimentary rocks nearby, which ultimately led to magnetite precipitation associated with the comb-layered quartz, K-feldspar, and biotite remnants on the contacts between the Heemskirk Granite and Neoproterozoic units at Granville Harbor (Figs. 3e and 4d).

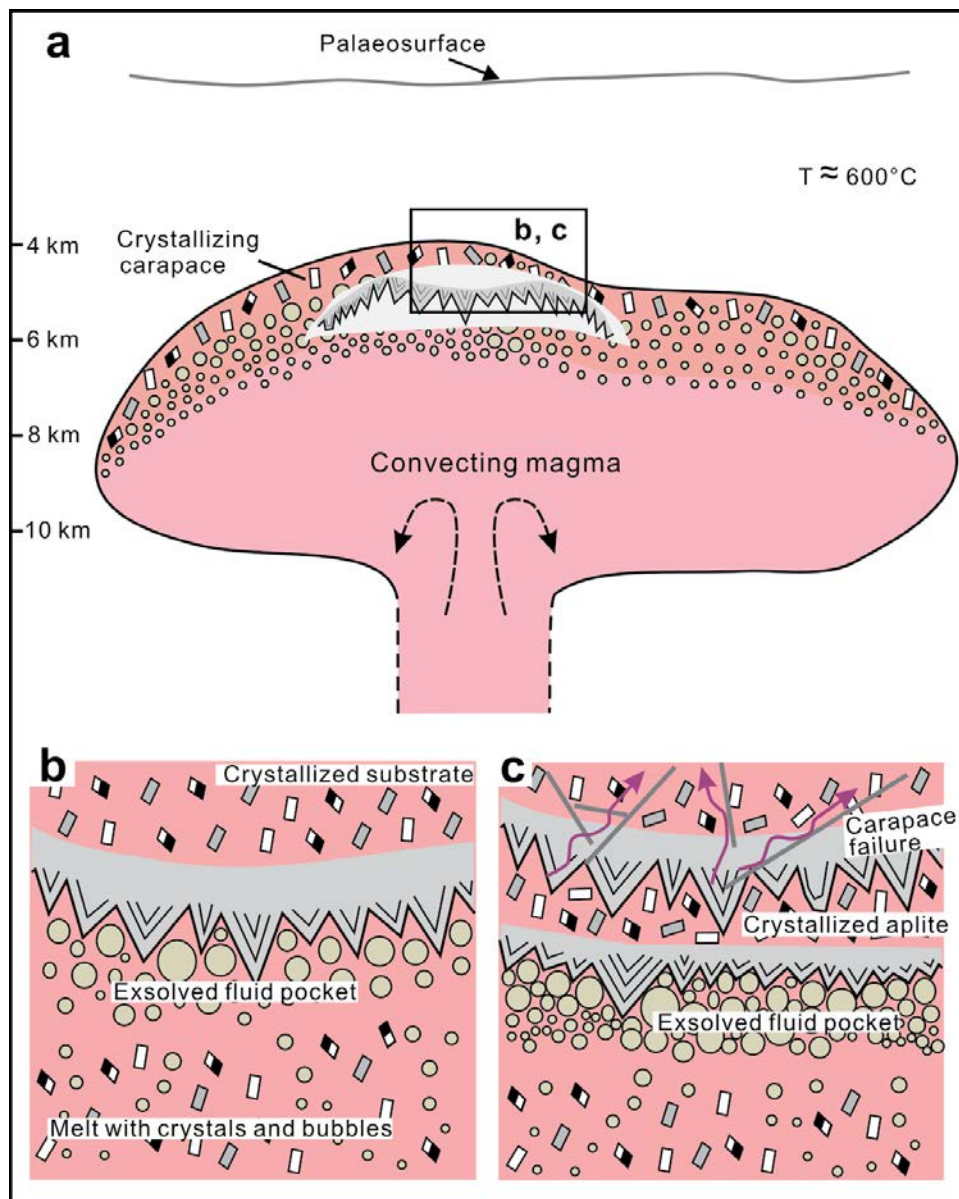The presence of multiple comb-quartz layers and aplite inter-

FIGURE 13. Schematic model showing the formation of quartz-rich unidirectional solidification textures at Heemskirk. (**a**) Exsolved volatile-rich aqueous fluids ascended to the crystallizing carapace during granitic melt emplaced into shallow crust (6–10 km), leading to the precipitation of multiple quartz-rich UST layers. (**b**) Volatiles bubbles accumulated in the roof zone, while quartz grew downward as USTs, with minor feldspar, biotite, and magnetite. (**c**) When vapor pressure exceeded the lithostatic load, brittle fracturing occurred, resulting in the release of aqueous fluids into overlying cupolas and the next cycles of growth of UST and intercalated aplite. (Color online.)

layers cut by K-feldspar muscovite seals (Fig. 3) provide physical evidence for fluctuating pressure conditions during granite crystallization, as the fluids exsolved from the silicate melt accumulated and escaped episodically during this process (Fig. 13). The brittle fracture caused drastic pressure drop coupled with heat loss via phase separation. Subsequent undercooling adjacent to the UST layers led to the crystallization of the aplite substrate that alternates with the comb layers (Fig. 13; Kirkham and Sinclair 1988; Lowenstern and Sinclair 1996). Open system conditions were transient, with minerals precipitating rapidly, sealing the brittle fractures that formed during decompression, allowing the next cycle of UST formation to commence (Fig. 13). Periodic pressure buildup and release continued until the vapor pressure could no longer fracture the carapace, ending the unidirectional solidification growth, with the remaining volatiles trapped as miarolitic cavities, pegmatites, discontinuous vein dikes, and/or tourmaline-quartz orbicules in the roof zones of the Heemskirk Granite (Hong et al. 2017b). The CL textures, trace-element compositions, and O-isotopic compositions of quartz (e.g., Figs. 5–7), as well as the textures and compositions of magnetite within USTs, are all consistent with the comb-layered USTs and quartz-filled miarolitic cavities in the Heemskirk Granite precipitating from volatile-rich, silica-saturated fluid pockets trapped in the carapace of the crystallizing felsic melts during the magmatic-hydrothermal transition (cf. Kirkham and Sinclair 1988; Carten et al. 1988; Candela and Blevin 1995; Lowenstern and Sinclair 1996; Harris et al. 2004; Hong et al. 2017b).

Significance for mineralization

Since euhedral crystal terminations of the comb-layer quartz point down toward the orientation of crystallization of the younger intrusion, Shannon et al. (1982) argued that recognition and detailed measurements of USTs could provide unambiguous evidence for relative age relationships among adjacent intrusions of similar composition. For example, the flat quartz-rich USTs that extend for hundreds of meters at Trial Harbor provide convincing evidence that the White phase of the Heemskirk Granite intruded the overlying Red phase granite (Fig. 3f). Recognition of these textures can, therefore, advance understanding of intrusive emplacement, magmatic crystallization, volatile exsolution, and magmatic aqueous fluid origination.

Unidirectional solidification textures are commonly associated with miarolitic cavities, vein dikes, saccharoidal quartz, and/or pegmatite pods within granitic stocks (Kirkham and Sinclair 1988; Candela and Blevin 1995; Lowenstern and Sinclair 1996; Lickfold et al. 2003; Harris et al. 2004; Breiter et al. 2005; Hong et al. 2017b). These distinctive textures typically occur in the apices of shallow-level granitoids, and can be associated with porphyry Cu, Au, Mo, and W deposits or granite-related Sn deposits (Shannon et al. 1982; Carten et al. 1988; Kirkham and Sinclair 1988; Lowenstern and Sinclair 1996; Kirwin and Seltmann 2002; Lickfold et al. 2003, 2007; Wilson et al. 2003; Harris et al. 2004; Cannell et al. 2005; Hong et al. 2017b). In porphyry deposits, zones of comb-layered quartz generally underlie the mineralized stockwork and form during the transitional stage prior to main-stage mineralization (Carten et al. 1988; Harris et al. 2004; Cannell et al. 2005). Minor coarse-grained sulfides occur locally in UST-layers, which may represent the earliest discernible mineralizing event (Lickfold et al. 2003). In the Northparkes porphyry Cu-Au deposits (New South Wales, Australia), abundant comb-quartz layers have been only observed in mineralized intrusions and not in barren intrusions (Lickfold et al. 2007). In western Tasmania, both the mineralized Heemskirk and barren Pieman Heads granites have similar tourmaline-rich features, but only the Heemskirk Granite has abundant quartz-rich USTs and miarolitic cavities (Hong et al. 2017b). Mineralized intrusions most likely experience a greater mass fractionation of fluids, volatiles, and metals than barren intrusions (cf. Lowenstern and Sinclair 1996). As a result, recognition and analysis of USTs can help to identify mineralized intrusions and provide encouragement for mineral exploration.

Implications

The study documents the textures and geochemistry of quartz and magnetite in solidification fronts in the carapace of the Heemskirk Granite from western Tasmania. Our SEM-CL, LA-ICP-MS, and O-isotopic analyses of quartz demonstrate that the comb-layered textures formed from magmatic-hydrothermal aqueous fluids (560–600 °C) that exsolved from silicic magma during its emplacement into the shallow crust (6–10 km, 1.3 kbar). Quartz-rich unidirectional solidification textures (USTs) can be easily mistaken for quartz veins, pegmatite, and stockscheider pods because of their megacrystic grain sizes. This study advances the understanding of USTs and related features that occur in the apical regions and/or walls of granitic intrusions worldwide. UST-quartz layers are geological indicators of granitoid that have economic potential. They also occur in the apical regions of granites associated with porphyry Cu-Au-Mo and W deposits but are postulated to have distinct chemical compositions, redox, and degrees of crystal fractionation from those associated with Sn-mineralized intrusions (cf. Blevin and Chappell 1995). Additional trace-element studies of UST quartz from different types of magmatic-hydrothermal ore deposits may provide a new tool for mineral exploration.

References Cited

Audétat, A., Garbe-Schönberg, D., Kronz, A., Pettke, T., Rusk, B., Donovan, J.J., and Lowers, H.A. (2015) Characterisation of a natural quartz crystal as a reference material for microanalytical determination of Ti, Al, Li, Fe, Mn, Ga and Ge. Geostandards and Geoanalytical Research, 39, 171–184.

Berry, R.F., and Crawford, A. (1988) The tectonic significance of Cambrian allochthonous mafic-ultramafic complexes in Tasmania. Australian Journal of Earth Sciences, 35, 523–533.

Black, L.P., McClenaghan, M.P., Korsch, R.J., Everard, J.L., and Foudoulis, C. (2005) Significance of Devonian–Carboniferous igneous activity in Tasmania as derived from U–Pb SHRIMP dating of zircon. Australian Journal of Earth Sciences, 52, 807–829.

Black, L.P., Everard, J.L., McClenaghan, M.P., Korsch, R.J., Calver, C.R., Fioretti, A.M., Brown, A.V., and Foudoulis, C. (2010) Controls on Devonian–Carboniferous magmatism in Tasmania, based on inherited zircon age patterns, Sr, Nd and Pb isotopes, and major and trace element geochemistry. Australian Journal of Earth Sciences, 57, 933–968.

Blevin, P.L., and Chappell, B.W. (1995) Chemistry, origin and evolution of mineralized

granites in the Lachlan Fold Belt, Australia: the metallogeny of I- and S-type granites. Economic Geology, 90, 1604–1619.

Both, R.A., and Williams, K.L. (1968) Mineralogical zoning in the lead-zinc ores of the Zeehan field, Tasmania Part I: Introduction and review. Journal of the Geological Society of Australia, 15, 121–137.

Breiter, K., Müller, A., Leichmann, J., and Gabašová, A. (2005) Textural and chemical evolution of a fractionated granitic system: the Podlesí stock, Czech Republic. Lithos, 80, 323–345.

Breiter, K., Ackerman, L., Svojtka, M., and Müller, A. (2013) Behavior of trace elements in quartz from plutons of different geochemical signature: A case study from the Bohemian Massif, Czech Republic. Lithos, 175-176, 54–67.

Burnham, C.W. (1979) Magmas and hydrothermal fluids. In H.L. Barnes, Ed., Geochemistry of Hydrothermal Ore Deposits, 2nd ed., p. 71–136. Wiley, New York.

Candela, P.A. (1991) Physics of aqueous phase evolution in plutonic environments. American Mineralogist, 76, 1081–1091.

——— (1997) A review of shallow, ore-related granites: textures, volatiles, and ore metals. Journal of Petrology, 38, 1619–1633.

Candela, P.A., and Blevin, P.L. (1995) Do some miarolitic granites preserve evidence of magmatic volatile phase permeability? Economic Geology, 90, 2310–2316.

Cannell, J., Cooke, D.R., Walshe, J.L., and Stein, H. (2005) Geology, mineralization, alteration and structural evolution of the El Teniente porphyry Cu-Mo deposit. Economic Geology, 100, 979–1003.

Carten, R.B., Geraghty, E.P., Walker, B.M., and Shannon, J.R. (1988) Cyclic development of igneous features and their relationship to high-temperature hydrothermal features in the Henderson porphyry molybdenum deposit, Colorado. Economic Geology, 83, 266–296.

Chappell, B.W., and White, A.J.R. (2001) Two contrasting granite types: 25 years later. Australian Journal of Earth Sciences, 48, 489–499.

Clayton, R.N., O'Neil, J.R., and Mayeda, T.K. (1972) Oxygen isotope exchange between quartz and water. Journal of Geophysical Research, 77, 3057–3067.

Corbett, K.D., Quilty, P.G., and Calver, C.R. (2014) Geological Evolution of Tasmania. 624 p. Geological Society of Australia, Special Publication 24.

Dare, S.A.S., Barnes, S.-J., Beaudoin, G., Méric, J., Boutroy, E., and Potvin-Doucet, C. (2014) Trace elements in magnetite as petrogenetic indicators. Mineralium Deposita, 49, 785–796.

Drivenes, K., Larsen, R.B., Müller, A., and Sørensen, B.E. (2016) Crystallization and uplift path of late Variscan granites evidenced by quartz chemistry and fluid inclusions: Example from the Land's End granite, SW England. Lithos, 252, 57–75.

Droop, G. (1987) A general equation for estimating Fe^{3+} concentrations in ferromagnesian silicates and oxides from microprobe analyses, using stoichiometric criteria. Mineralogical Magazine, 51, 431–435.

Dupuis, C., and Beaudoin, G. (2011) Discriminant diagrams for iron oxide trace element fingerprinting of mineral deposit types. Mineralium Deposita, 46, 319–335.

Fayek, M., Harrison, T.M., Ewing, R.C., Grove, M., and Coath, C.D. (2002) O and Pb isotopic analyses of uranium minerals by ion microprobe and U–Pb ages from the Cigar Lake deposit. Chemical Geology, 185, 205–225.

Götze, J., Plötze, M., Graupner, T., Hallbauer, D.K., and Bray, C.J. (2004) Trace element incorporation into quartz: A combined study by ICP-MS, electron spin resonance, cathodoluminescence, capillary ion analysis, and gas chromatography. Geochimica et Cosmochimica Acta, 68, 3741–3759.

Hajitaheri, J. (1985) The origin of mineralisation in South Heemskirk Granite, western Tasmania, Australia, p. 322. Ph.D. thesis, University of Tasmania, Hobart.

Halpin, J.A., Jensen, T., McGoldrick, P., Meffre, S., Berry, R.F., Everard, J.L., Calver, C.R., Thompson, J., Goemann, K., and Whittaker, J.M. (2014) Authigenic monazite and detrital zircon dating from the Proterozoic Rocky Cape Group, Tasmania: Links to the Belt-Purcell Supergroup, North America. Precambrian Research, 250, 50–67.

Harris, A.C., Kamenetsky, V.S., White, N.C., and Steele, D.A. (2004) Volatile phase separation in silicic magmas at Bajo de la Alumbrera porphyry Cu-Au deposit, NW Argentina. Resource Geology, 54, 341–356.

Harris, A.C., Cuison, A.L.G., Chang, Z., Cooke, D.R., Bonnici, N., Faure, K., and Cross, C. (2007) Fe-rich magmatic volatiles in the Ridgeway Au-Cu porphyries: evidence from magnetite-quartz comb-layered textures. In C.J. Andrew, Ed., Digging Deeper, p. 415–418. Proceedings of the 9th Biennial SGA Meeting, Dublin.

Hedenquist, J.W., and Lowenstern, J.B. (1994) The role of magmas in the formation of hydrothermal ore deposits. Nature, 370, 519–527.

Hoefs, J. (2009) Stable Isotope Geochemistry, 6th ed., p. 115–116. Springer.

Hong, W. (2016) Magmatic-hydrothermal volatile exsolution and mineralisation in Tasmanian Sn granites, p. 212. Ph.D. thesis. University of Tasmania, Hobart.

Hong, W., Cooke, D.R., Huston, D.L., Maas, R., Meffre, S., Thompson, J., Zhang, L., and Fox, N. (2017a) Geochronological, geochemical and Pb isotopic compositions of Tasmanian granites (southeast Australia): Controls on petrogenesis, geodynamic evolution and tin mineralisation. Gondwana Research, 46, 124–140.

Hong, W., Cooke, D.R., Zhang, L., Fox, N., and Thompson, J. (2017b) Tourmaline-rich features in the Heemskirk and Pieman Heads granites from western Tasmania, Australia: Characteristics, origins, and implications for tin mineralization. American Mineralogist, 102, 876–899.

Huang, R., and Audétat, A. (2012) The titanium-in-quartz (TitaniQ) thermobarometer: a critical examination and re-calibration. Geochimica et Cosmochimica Acta, 84, 75–89.

Ishihara, S. (1977) The magnetite-series and ilmenite-series granitic rocks. Mining

Geology, 27, 293–305.

Keays, R.R., and Jowitt, S.M. (2013) The Avebury Ni deposit, Tasmania: A case study of an unconventional nickel deposit. Ore Geology Reviews, 52, 4–17.

Kirkham, R.V., and Sinclair, W.D. (1988) Comb quartz layers in felsic intrusions and their relationship to porphyry deposits. In R.R. Taylor, and D.F. Strong, Eds., Recent Advances in the Geology of Granite-Related Mineral Deposits, 31, 50–71. Canadian Institute of Mining and Metallurgy, Special Volume.

Kirwin, D.J., and Seltmann, R. (2002) Unidirectional solidification textures associated with intrusion-related gold deposits. 11th Quadrennial IAGOD Symposium and Geocongress, 22–26.

Large, R.R. (1992) Australian volcanic-hosted massive sulfide deposits; features, styles, and genetic models. Economic Geology, 87, 471–510.

Larsen, R.B., Henderson, I., Ihlen, P.M., and Jacamon, F. (2004) Distribution and petrogenetic behaviour of trace elements in granitic pegmatite quartz from South Norway. Contributions to Mineralogy and Petrology, 147, 615–628.

Leaman, D.E., and Richardson, R.G. (2003) A geophysical model of the major Tasmanian granitoids. Mineral Resources Tasmania, Tasmanian Geological Survey Record 2003/11, 1–8.

Lickfold, V., Cooke, D.R., Smith, S.G., and Ullrich, T.D. (2003) Endeavour copper-gold porphyry deposits, Northparkes, New South Wales: Intrusive history and fluid evolution. Economic Geology, 98, 1607–1636.

Lickfold, V., Cooke, D.R., Crawford, A.J., and Fanning, C.M. (2007) Shoshonitic magmatism and the formation of the Northparkes porphyry Cu–Au deposits, New South Wales. Australian Journal of Earth Sciences, 54, 417–444.

Lowenstern, J.B., and Sinclair, W.D. (1996) Exsolved magmatic fluid and its role in the formation of comb-layered quartz at the Cretaceous Logtung W-Mo deposit, Yukon Territory, Canada. Transactions of the Royal Society of Edinburgh: Earth Sciences, 87, 291–303.

McClenaghan, M.P. (2006) The geochemistry of Tasmanian Devonian-Carboniferous granites and implications for the composition of their source rocks, p. 1–31. Mineral Resources Tasmania, Tasmanian Geological Survey Record 2006/06.

Müller, A., Herrington, R., Armstrong, R., Seltmann, R., Kirwin, D.J., Stenina, N.G., and Kronz, A. (2010) Trace elements and cathodoluminescence of quartz in stockwork veins of Mongolian porphyry-style deposits. Mineralium Deposita, 45, 707–727.

Nadoll, P., Angerer, T., Mauk, J.L., French, D., and Walshe, J. (2014) The chemistry of hydrothermal magnetite: A review. Ore Geology Reviews, 61, 1–32.

Nadoll, P., Mauk, J.L., Leveille, R.A., and Koenig, A.E. (2015) Geochemistry of magnetite from porphyry Cu and skarn deposits in the southwestern United States. Mineralium Deposita, 50, 493–515.

Ostapenko, G.T., Tarashchan, A.N., and Mitsyuk, B.M. (2007) Rutile-quartz geothermobarometer. Geochemistry International, 45, 506–508.

Rusk, B.G., Lowers, H.A., and Reed, M.H. (2008) Trace elements in hydrothermal quartz: Relationships to cathodoluminescent textures and insights into vein formation. Geology, 36, 547–550.

Rusk, B., Koenig, A., and Lowers, H. (2011) Visualizing trace element distribution in quartz using cathodoluminescence, electron microprobe, and laser ablation-inductively coupled plasma-mass spectrometry. American Mineralogist, 96, 703–708.

Schmitz, C., and Burt, D.M. (1990) The Black Pearl mine, Arizona; Wolframite veins and stockscheider pegmatite related to an albitic stock. Geological Society of America Special Papers, 246, 221–232.

Seymour, D.B., Green, G.R., and Calver, C.R. (2007) The geological and mineral deposits of Tasmania: a summary, 1–29. Tasmanian Geological Survey Bulletin 72.

Shannon, J.R., Walker, B.M., Carten, R.B., and Geraghty, E.P. (1982) Unidirectional solidification textures and their significance in determining relative ages of intrusions at the Henderson Mine, Colorado. Geology, 10, 293–297.

Tanner, D., Henley, R.W., Mavrogenes, J.A., and Holden, P. (2013) Combining in situ isotopic, trace element and textural analyses of quartz from four magmatic-hydrothermal ore deposits. Contributions to Mineralogy and Petrology, 166, 1119–1142.

Taylor, H.P. Jr. (1974) The application of oxygen and hydrogen isotope studies to problems of hydrothermal alteration and ore deposition. Economic Geology, 69, 843–883.

Thomas, J.B., Watson, E.B., Spear, F.S., Shemella, P.T., Nayak, S.K., and Lanzirotti, A. (2010) TitaniQ under pressure: the effect of pressure and temperature on the solubility of Ti in quartz. Contributions to Mineralogy and Petrology, 160, 743–759.

Wark, D.A., and Watson, E.B. (2006) TitaniQ: a titanium-in-quartz geothermometer. Contributions to Mineralogy and Petrology, 152, 743–754.

Wilson, A.J., Cooke, D.R., and Happer, B.L. (2003) The Ridgeway gold-copper deposit: A high-grade alkalic porphyry deposit in the Lachlan Fold Belt, New South Wales, Australia. Economic Geology, 98, 1637–1666.

Endnote:

[1]Deposit item AM-19-16534, Supplemental Material. Deposit items are free to all readers and found on the MSA web site, via the specific issue's Table of Contents (go to http://www.minsocam.org/MSA/AmMin/TOC/2019/Jan2019_data/Jan2019_data.html).